

## TOPOLOGICAL MATTER

# Evidence for Majorana bound states in an iron-based superconductor

Dongfei Wang<sup>1,2\*</sup>, Lingyuan Kong<sup>1,2\*</sup>, Peng Fan<sup>1,2\*</sup>, Hui Chen<sup>1</sup>, Shiyu Zhu<sup>1,2</sup>, Wenyao Liu<sup>1,2</sup>, Lu Cao<sup>1,2</sup>, Yujie Sun<sup>1,3</sup>, Shixuan Du<sup>1,3,4</sup>, John Schneeloch<sup>5</sup>, Ruidan Zhong<sup>5</sup>, Genda Gu<sup>5</sup>, Liang Fu<sup>6</sup>, Hong Ding<sup>1,2,3,4,†</sup>, Hong-Jun Gao<sup>1,2,3,4,†</sup>

The search for Majorana bound states (MBSs) has been fueled by the prospect of using their non-Abelian statistics for robust quantum computation. Two-dimensional superconducting topological materials have been predicted to host MBSs as zero-energy modes in vortex cores. By using scanning tunneling spectroscopy on the superconducting Dirac surface state of the iron-based superconductor  $\text{FeTe}_{0.55}\text{Se}_{0.45}$ , we observed a sharp zero-bias peak inside a vortex core that does not split when moving away from the vortex center. The evolution of the peak under varying magnetic field, temperature, and tunneling barrier is consistent with the tunneling to a nearly pure MBS, separated from nontopological bound states. This observation offers a potential platform for realizing and manipulating MBSs at a relatively high temperature.

Majorana bound states (MBSs) in condensed-matter systems have attracted tremendous interest owing to their non-Abelian statistics and potential applications in topological quantum computation (1, 2). A MBS is theoretically predicted to emerge as a spatially localized zero-energy mode in certain  $p$ -wave topological superconductors in one and two dimensions (3, 4). Although the material realization of such  $p$ -wave superconductors has remained elusive, other platforms for MBSs have recently been proposed, using heterostructures between conventional  $s$ -wave superconductors and topological insulators (5), nanowires (6–8), quantum anomalous Hall insulators (9), or atomic chains (10), where the proximity effect on a spin-nondegenerate band creates a superconducting (SC) topological state. Various experimental signatures of MBSs (11–14) or Majorana chiral modes (15) have been observed in these heterostructures, but clear detection and manipulation of MBSs are often hindered by the contribution of nontopological bound states and complications of material interface.

Very recently, using high-resolution angle-resolved photoemission spectroscopy (ARPES), a potential platform for MBSs was discovered in the bulk superconductor  $\text{FeTe}_{0.55}\text{Se}_{0.45}$ , with a SC transition temperature  $T_c = 14.5$  K and a simple crystal structure (Fig. 1A). Because of the topological band inversion between the  $p_z$  and  $d_{xz}/d_{yz}$

bands around the  $\bar{\Gamma}$  point (16, 17) and the multi-band nature (Fig. 1B), this single material naturally has a spin-helical Dirac surface state, with an induced full SC gap and a small Fermi energy (Fig. 1C) (18); these properties would create favorable conditions for observing a pure MBS (5) that is isolated from other nontopological Caroli-de Gennes-Matricorn bound states (CBSs) (19, 20). The combination of high- $T_c$  superconductivity and Dirac surface states in a single material removes the

challenging interface problems in previous proposals and offers clear advantages for the detection and manipulation of MBSs.

Motivated by the above considerations, we carried out a high-resolution scanning tunneling microscopy/spectroscopy (STM/S) experiment on the surface of  $\text{FeTe}_{0.55}\text{Se}_{0.45}$ , which has a good atomic resolution that reveals the lattice formed by Te/Se atoms on the surface (Fig. 1D). We started with a relatively low magnetic field of 0.5 T along the  $c$  axis at a low temperature of 0.55 K, with a clear observation of vortex cores in Fig. 1E. At the vortex center, we observed a strong zero-bias peak (ZBP) with a full width at half maximum (FWHM) of 0.3 meV and an amplitude of 2 relative to the intensity just outside the gapped region. Outside of the vortex core, we clearly observed a SC spectrum with multiple gap features, similar to the ones observed in previous STM studies on the same material (21, 22). These different SC gaps correspond well with the SC gaps on different Fermi surfaces of this material observed in previous ARPES studies (table S1) (23, 24). A similar ZBP was reported previously (22).

We next demonstrate in Fig. 2 and fig. S4 (24) that across a large range of magnetic fields, the observed ZBP does not split when moving away from a vortex center. It can be clearly seen from Fig. 2, A to D, that the ZBP remains at the zero energy, while its intensity fades away when moving away from the vortex center. The nonsplit ZBP contrasts sharply with the split ZBP originating from CBS observed in conventional superconductors

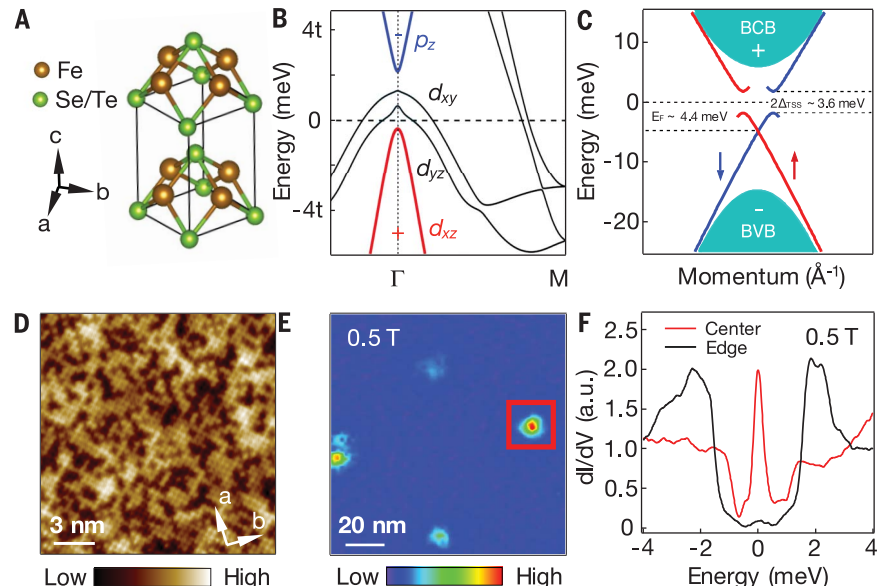


**Fig. 1. Band structure and vortex cores of  $\text{FeTe}_{0.55}\text{Se}_{0.45}$ .** (A) Crystal structure of  $\text{FeTe}_{0.55}\text{Se}_{0.45}$ . Axis  $a$  or  $b$  indicates one of the Fe–Fe bond directions. (B) A first-principle calculation of the band structure along the  $\Gamma$ – $M$  direction. In the calculations,  $t = 100$  meV, whereas  $t \sim 12$  to 25 meV from ARPES experiments, largely depending on the bands (23). [Adapted from (18), figure 1C] (C) Summary of SC topological surface states on this material observed by ARPES from (18). (D) STM topography of  $\text{FeTe}_{0.55}\text{Se}_{0.45}$  (scanning area, 17 nm by 17 nm). (E) Normalized zero-bias conductance (ZBC) map measured at a magnetic field of 0.5 T, with the area 120 nm by 120 nm. (F) A sharp ZBP in a  $dI/dV$  spectrum measured at the vortex core center indicated in the red box in (E). Settings are sample bias,  $V_s = -5$  mV; tunneling current,  $I_t = 200$  pA; and temperature,  $T = 0.55$  K.

<sup>1</sup>Beijing National Laboratory for Condensed Matter Physics and Institute of Physics, Chinese Academy of Sciences (CAS), Beijing 100190, China. <sup>2</sup>School of Physical Sciences, University of Chinese Academy of Sciences, Beijing 100190, China. <sup>3</sup>CAS Center for Excellence in Topological Quantum Computation, University of Chinese Academy of Sciences, Beijing 100190, China. <sup>4</sup>Collaborative Innovation Center of Quantum Matter, Beijing 100190, China. <sup>5</sup>Condensed Matter Physics and Materials Science Department, Brookhaven National Laboratory, Upton, NY 11973, USA. <sup>6</sup>Department of Physics, Massachusetts Institute of Technology, Cambridge, MA 02139, USA.

\*These authors contributed equally to this work.

†Corresponding author. Email: dingh@iphy.ac.cn (H.D.); hjgao@iphy.ac.cn (H.-J.G.)

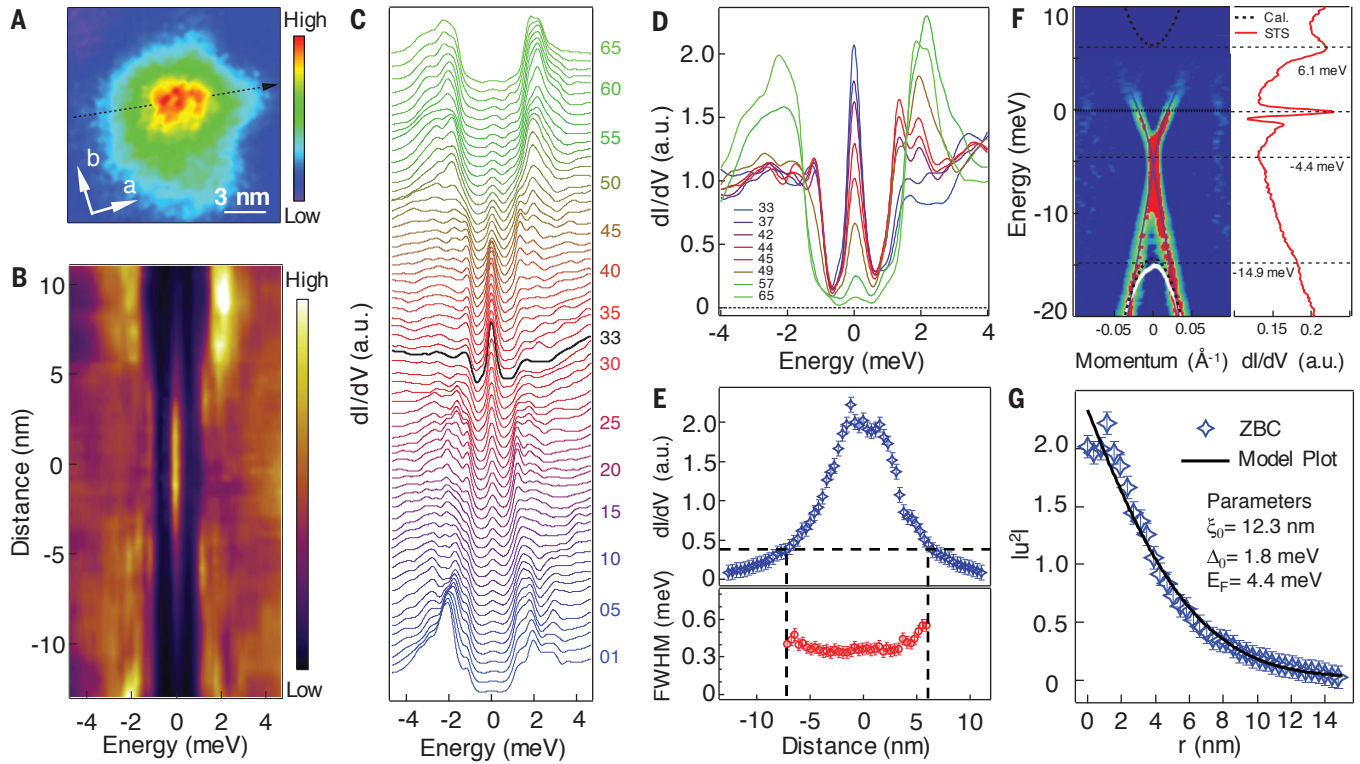


**Fig. 2. Energetic and spatial profile of ZBPs.** (A) A ZBC map (area, 15 nm by 15 nm) around vortex cores. (B) A line-cut intensity plot along the black dashed line indicated in (A). (C) A waterfall-like plot of (B) with 65 spectra, with the black curve corresponding to the one in the core center. (D) An overlapping display of eight  $dI/dV$  spectra selected from (C). (E) Spatial dependence of the height (top) and FWHM (bottom) of the ZBP. (F) Comparison between ARPES and STS results. (Left) ARPES results on the topological surface states. [Adapted from (18)] Black dashed

curves are extracted from a first-principle calculation (37), with the calculated data rescaled to match the energy positions of the Dirac point and the top of the bulk valence band (BVB). (Right) A  $dI/dV$  spectrum measured from  $-20$  to  $10$  meV. (G) Comparison between the measured ZBP peak intensity with a theoretical calculation of MBS spatial profile [(24), part VIII]. The data in (B) to (G) are normalized by the integrated area of each  $dI/dV$  spectrum. Settings are  $V_s = -5$  mV,  $I_t = 200$  pA,  $T = 0.55$  K, and perpendicular magnetic field ( $B_{\perp}$ ) =  $0.5$  T.

(19, 20) and is consistent with tunneling into an isolated MBS in a vortex core of a SC topological material (5, 25–27). We then extracted the position-dependent values of the ZBP height and width using simple Gaussian fits of the data in Fig. 2C and obtained the spatial profile shown in Fig. 2E; the decaying profile has a nearly constant line width of  $\sim 0.3$  meV in the center, which is close to the total width ( $\sim 0.28$  meV) contributed from the STM energy resolution [ $\sim 0.23$  meV as shown in part I of (24)] and the thermal broadening [ $3.5k_B T$  at  $0.55$  K  $\sim 0.17$  meV, where  $k_B$  is the Boltzmann constant]. We further compared the observed ZBP height with a theoretical MBS spatial profile obtained by solving the Bogoliubov–de Gennes equation analytically (5, 25) or numerically (26, 27). By using the parameters of  $E_F = 4.4$  meV,  $\Delta_{sc} = 1.8$  meV, and  $\xi_0 = v_F/\Delta_{sc} = 12$  nm, which are obtained directly from the topological surface state by our scanning tunneling spectroscopy (STS) and ARPES results (Fig. 2F) (18), the theoretical MBS profile matches well the experimental one (Fig. 2G).

The observation of a nonsplit ZBP, which is different from the split ZBP observed in a vortex of the  $\text{Bi}_2\text{Te}_3/\text{NbSe}_2$  heterostructure (13, 28, 29), indicates that the MBS peak in our system is much less contaminated by nontopological CBS peaks,

which is made possible by the large  $\Delta_{sc}/E_F$  ratio in this system. In a usual topological insulator/superconductor heterostructure, this ratio is tiny, on the order of  $10^{-3}$  to  $10^{-2}$  (28). This has been shown to induce, in addition to the MBS at the zero energy, many CBSs, whose level spacing is proportional to  $\Delta_{sc}^2/E_F$ . As a result, these CBSs were crowded together very close to the zero energy, making difficult a clean detection of MBS from the  $dI/dV$  spectra (29). However, on the surface of  $\text{FeTe}_{0.55}\text{Se}_{0.45}$ , the value of  $\Delta_{sc}^2/E_F$  is  $\sim 0.74$  meV, which is sufficiently large to push most CBSs away from the zero energy (24), leaving the MBS largely isolated and unspoiled. A large energy separation (0.7 meV) between the ZBP and the CBS was observed in fig. S3, E to H, which is in agreement with  $\Delta_{sc}^2/E_F$  of the topological surface states [(24), part IV]. Also, all the bulk bands in this multiband material have fairly small values of  $E_F$  owing to large correlation-induced mass renormalization, ranging from a few to a few tens of millielectron volts; thus, their values of  $\Delta_{sc}^2/E_F$  are also quite large ( $>0.2$  meV) (table S1) (24). These large bulk ratios enlarge the energy-level spacing of CBSs inside the bulk vortex line, which helps reduce quasiparticle poisoning of the MBS at low temperature [(24), part II].

It has been predicted (30) that the width of the ZBP from tunneling into a single isolated MBS is determined by thermal smearing ( $3.5k_B T$ ), tunneling broadening, and STM instrumentation resolution. We measured the tunneling barrier evolution of the ZBP (Fig. 3A). Robust ZBPs can be observed over two orders of magnitude in tunneling barrier conductance, with the width barely changing (Fig. 3B). Also, the line width of ZBPs is almost completely limited by the combined broadening of energy resolution and STM thermal effect, suggesting that the intrinsic width of the MBS is much smaller, and our measurements are within the weak tunneling regime.

However, we did observe some other ZBPs with a larger broadening (Fig. 3C). A larger ZBP broadening is usually accompanied with a softer SC gap, or the FWHM of ZBP increases with increasing subgap background conductance. The subgap background conductance, which is determined by factors such as the strength of scattering from disorder and quasiparticle interactions (31–33), introduces a gapless fermion bath that can poison the MBS, as explained previously (34). The effect of quasiparticle poisoning is to reduce the MBS amplitude and increase its width. This scenario is likely the origin of a

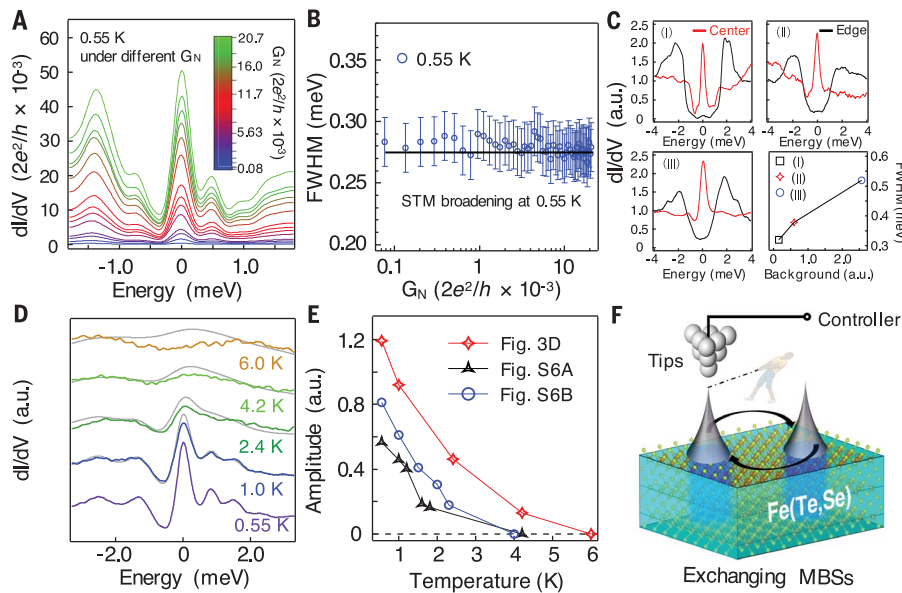


**Fig. 3. Temperature and tunneling barrier evolution of ZBPs.** (A) Evolution of ZBPs, with tunneling barrier measured at 0.55 K.  $G_N \equiv I_t/V_s$ , which corresponds to the energy-averaged conductance of normal states and represents the conductance of the tunneling barrier.  $I_t$  and  $V_s$  are the STS setpoint parameters. (B) FWHM of ZBPs at 0.55 K under different tunneling barriers. The black solid line is the combined effect of energy resolution (0.23 meV) (24) and tip thermal broadening ( $3.5k_B T$ ) at 0.55 K. (C) FWHM of ZBP at the center of the vortex core is larger when the SC gap around the vortex core is softer. Background is defined as an integrated area from  $-1$  to  $+1$  meV of the spectra at the core edge. (D) Temperature evolution of ZBPs in a vortex core. The gray curves are numerically broadened 0.55 K data at each temperature. (E) Amplitude of the ZBPs shown in (D) and fig. S6 (24) under different temperatures. The amplitude is defined as the peak-valley difference of the ZBP. (F) Schematic of a possible way for realizing non-Abelian statistics in an ultralow-temperature STM experiment that may have an ability to exchange MBSs on the surface of Fe(Te, Se). (A) and (B) show the absolute value of conductance;  $B_{\perp} = 2.5$  T. In (D) and (E), the data are normalized by integrated area;  $V_s = -10$  mV,  $I_t = 100$  pA,  $T = 0.55$  K, and  $B_{\perp} = 4$  T.

larger broadening of ZBP accompanied by a softer gap.

It has been pointed out by previous theoretical studies (35–37) that the condition of a bulk vortex line, such as its chemical potential, has substantial influences on the Majorana mode on the surface by the vortex phase transition. In order to further characterize the effects of bulk vortex lines, we have monitored the temperature evolution of a ZBP. As shown in Fig. 3D, the ZBP intensity measured at a vortex center decreases with increasing temperature and becomes extremely weak at 4.2 K and totally invisible at 6.0 K. A peak associated with a CBS would persist to higher temperatures and exhibit simple Fermi-Dirac broadening up to about  $T_c/2$  ( $\sim 8$  K), below which the SC gap amplitude is almost constant, as observed in our previous ARPES measurement (18). Our observation (Fig. 3D) contradicts this expectation and indicates an additional suppression mechanism that is likely related to the poisoning of MBS by thermally excited quasiparticles. From the extraction of ZBP amplitude measured on several different vortices (three cases are shown in Fig. 3E), we found that most of the observed ZBPs vanish around 3 K, which is higher than the temperature in many previous Majorana platforms (11, 38). This vanishing temperature is comparable with the energy

level spacing of the bulk vortex line as discussed above; thus, the temperature dependence we found is consistent with a case of a MBS poisoned by thermally induced quasiparticles inside the bulk vortex line (24).

Our observations provide strong evidence for tunneling to an isolated MBS; many alternative trivial explanations [(24), part III] cannot account for all the observed features. It is technically possible to move a vortex by a STM tip, which in principle can be used to exchange MBSs inside vortices (Fig. 3F), consequently demonstrating non-Abelian statistics under a sufficiently low ( $k_B T \ll \Delta_{sc}^2/E_F$ ) temperature (2). The high transition temperature and large SC gaps in this superconductor offer a promising platform to fabricate robust devices for topological quantum computation.

#### REFERENCES AND NOTES

1. A. Y. Kitaev, *Ann. Phys.* **303**, 2–30 (2003).
2. C. Nayak, S. H. Simon, A. Stern, M. Freedman, S. Das Sarma, *Rev. Mod. Phys.* **80**, 1083–1159 (2008).
3. A. Y. Kitaev, *Phys. Uspekhi* **44** (10S), 131–136 (2001).
4. N. Read, D. Green, *Phys. Rev. B* **61**, 10267–10297 (2000).
5. L. Fu, C. L. Kane, *Phys. Rev. Lett.* **100**, 096407 (2008).
6. R. M. Lutchyn, J. D. Sau, S. Das Sarma, *Phys. Rev. Lett.* **105**, 077001 (2010).
7. Y. Oreg, G. Refael, F. von Oppen, *Phys. Rev. Lett.* **105**, 177002 (2010).

8. A. C. Potter, P. A. Lee, *Phys. Rev. Lett.* **105**, 227003 (2010).
9. X.-L. Qi, T. L. Hughes, S.-C. Zhang, *Phys. Rev. B* **82**, 184516 (2010).
10. S. Nadj-Perge, I. K. Drozdov, B. A. Bernevig, A. Yazdani, *Phys. Rev. B* **88**, 020407 (2013).
11. V. Mourik et al., *Science* **336**, 1003–1007 (2012).
12. S. Nadj-Perge et al., *Science* **346**, 602–607 (2014).
13. H.-H. Sun et al., *Phys. Rev. Lett.* **116**, 257003 (2016).
14. M. T. Deng et al., *Science* **354**, 1557–1562 (2016).
15. Q.-L. He et al., *Science* **357**, 294–299 (2017).
16. Z.-J. Wang et al., *Phys. Rev. B* **92**, 115119 (2015).
17. X.-X. Wu, S. Qin, Y. Liang, H. Fan, J. Hu, *Phys. Rev. B* **93**, 115129 (2016).
18. P. Zhang et al., *Science* **360**, 182–186 (2018).
19. C. Caroli, P. G. de Gennes, J. Matricon, *Phys. Lett.* **9**, 307–309 (1964).
20. H. F. Hess, R. B. Robinson, J. V. Waszczak, *Phys. Rev. Lett.* **64**, 2711–2714 (1990).
21. T. Hanaguri, S. Niihata, K. Kuroki, H. Takagi, *Science* **328**, 474–476 (2010).
22. F. Masee et al., *Sci. Adv.* **1**, e1500033 (2015).
23. H. Miao et al., *Phys. Rev. B* **85**, 094506 (2012).
24. Materials and methods are available as supplementary materials.
25. Y. Wang, L. Fu, *Phys. Rev. Lett.* **119**, 187003 (2017).
26. C.-K. Chiu, M. J. Gilbert, T. L. Hughes, *Phys. Rev. B* **84**, 144507 (2011).
27. L.-H. Hu, C. Li, D.-H. Xu, Y. Zhou, F.-C. Zhang, *Phys. Rev. B* **94**, 224501 (2016).
28. J.-P. Xu et al., *Phys. Rev. Lett.* **112**, 217001 (2014).
29. J.-P. Xu et al., *Phys. Rev. Lett.* **114**, 017001 (2015).
30. F. Setiawan, C.-X. Liu, J. D. Sau, S. Das Sarma, *Phys. Rev. B* **96**, 184520 (2017).
31. S. Das Sarma, A. Nag, J. D. Sau, *Phys. Rev. B* **94**, 035143 (2016).
32. Y. Yin et al., *Phys. Rev. Lett.* **102**, 097002 (2009).
33. C. Renner, A. D. Kent, P. Niedermann, O. Fischer, F. Lévy, *Phys. Rev. Lett.* **67**, 1650–1652 (1991).
34. J. R. Colbert, P. A. Lee, *Phys. Rev. B* **89**, 140505 (2014).
35. P. Hosur, P. Ghaemi, R. S. K. Mong, A. Vishwanath, *Phys. Rev. Lett.* **107**, 097001 (2011).
36. H.-H. Hung, P. Ghaemi, T. L. Hughes, M. J. Gilbert, *Phys. Rev. B* **87**, 035401 (2013).
37. G. Xu, B. Lian, P. Tang, X.-L. Qi, S.-C. Zhang, *Phys. Rev. Lett.* **117**, 047001 (2016).
38. F. Nichele et al., *Phys. Rev. Lett.* **119**, 136803 (2017).

#### ACKNOWLEDGMENTS

We thank Q. Huan, H. Isobe, X. Lin, X. Wu, and K. Yang for technical assistance and P. A. Lee, T. K. Ng, S. H. Pan, G. Xu, J.-X. Yin, F. C. Zhang, and P. Zhang for useful discussions. **Funding:** This work at IOP is supported by grants from the Ministry of Science and Technology of China (2013CBA01600, 2015CB921000, 2015CB921300, and 2016YFA0202300), the National Natural Science Foundation of China (11234014, 11574371, and 61390501), and the Chinese Academy of Sciences (XDPB08-1, XDB07000000, and XDPB0601). L.F. and G.G. are supported by the U.S. Department of Energy (DOE) (DE-SC0010526 and DE-SC0012704, respectively). J.S. and R.Z. are supported by the Center for Emergent Superconductivity, an Energy Frontier Research Center funded by the U.S. DOE. **Author contributions:** H.D., H.-J.G., L.K., Y.S., and S.D. designed the experiments. D.W., L.K., P.F., H.C., S.Z., W.L., and L.C. performed the STM experiments. J.S., R.Z., and G.G. provided the samples. L.F. provided theoretical models and explanations. All the authors participated in analyzing the experimental data, plotting the figures, and writing the manuscript. H.D. and H.-J.G. supervised the project. **Competing interests:** The authors declare that they have no competing interests. **Data and materials availability:** The data presented in this paper can be found in the supplementary materials.

#### SUPPLEMENTARY MATERIALS

www.sciencemag.org/content/362/6412/333/suppl/DC1  
Materials and Methods  
Supplementary Text  
Figs. S1 to S7  
Table S1  
References (39–69)  
Data File S1

22 June 2017; resubmitted 11 December 2017  
Accepted 27 July 2018  
Published online 16 August 2018  
10.1126/science.aao1797

## Evidence for Majorana bound states in an iron-based superconductor

Dongfei Wang, Lingyuan Kong, Peng Fan, Hui Chen, Shiyu Zhu, Wenyao Liu, Lu Cao, Yujie Sun, Shixuan Du, John Schneeloch, Ruidan Zhong, Genda Gu, Liang Fu, Hong Ding and Hong-Jun Gao

*Science* **362** (6412), 333-335.  
DOI: 10.1126/science.aao1797 originally published online August 16, 2018

### An iron home for Majoranas

The surface of the iron-based superconductor  $\text{FeTe}_{0.55}\text{Se}_{0.45}$  has been identified as a potential topological superconductor and is expected to host exotic quasiparticles called the Majorana bound states (MBSs). Wang *et al.* looked for signatures of MBSs in this material by using scanning tunneling spectroscopy on the vortex cores formed by the application of a magnetic field. In addition to conventional states, they observed the characteristic zero-bias peaks associated with MBSs and were able to distinguish between the two, owing to the favorable ratios of energy scales in the system.

*Science*, this issue p. 333

#### ARTICLE TOOLS

<http://science.sciencemag.org/content/362/6412/333>

#### SUPPLEMENTARY MATERIALS

<http://science.sciencemag.org/content/suppl/2018/08/15/science.aao1797.DC1>

#### REFERENCES

This article cites 68 articles, 9 of which you can access for free  
<http://science.sciencemag.org/content/362/6412/333#BIBL>

#### PERMISSIONS

<http://www.sciencemag.org/help/reprints-and-permissions>

Use of this article is subject to the [Terms of Service](#)



[www.sciencemag.org/cgi/content/full/science.aao1797/DC1](http://www.sciencemag.org/cgi/content/full/science.aao1797/DC1)

## Supplementary Material for

### **Evidence for Majorana bound states in an iron-based superconductor**

Dongfei Wang, Lingyuan Kong, Peng Fan, Hui Chen, Shiyu Zhu, Wenyao Liu, Lu Cao, Yujie Sun, Shixuan Du, John Schneeloch, Ruidan Zhong, Genda Gu, Liang Fu, Hong Ding\*, Hong-Jun Gao\*

\*Corresponding author. Email: [dingh@iphy.ac.cn](mailto:dingh@iphy.ac.cn) (H.D.); [hjgao@iphy.ac.cn](mailto:hjgao@iphy.ac.cn) (H.-J.G.)

Published 16 August 2018 as *Science* First Release  
DOI: 10.1126/science.aao1797

#### **This PDF file includes:**

Materials and Methods  
Supplementary Text  
Figs. S1 to S7  
Table S1  
References

**Other Supplementary Material for this manuscript includes the following:**  
(available at [www.sciencemag.org/content/science.aao1797/DC1](http://www.sciencemag.org/content/science.aao1797/DC1))

Data File S1 as a separate .zip file

## Materials and Methods:

Large single crystals of  $\text{FeTe}_{0.55}\text{Se}_{0.45}$  with high quality were grown using the self-flux method, and their values of  $T_c$  were determined to be 14.5 K from magnetization measurements (39). There are two kinds of single crystals crystalizing simultaneously with similar structure and Te/Se compositions.  $\text{Fe}_{1+y}\text{Te}_{0.55}\text{Se}_{0.45}$  single crystals with excess Fe atoms, with shinning surfaces and being easy to cleave, are non-superconducting before annealing under Te atmosphere.  $\text{FeTe}_{0.55}\text{Se}_{0.45}$  single crystals without excess Fe, usually without shinning surface, are superconducting without post-annealing. All STM/STS data shown in this paper are from as-grown  $\text{FeTe}_{0.55}\text{Se}_{0.45}$  single crystals, and previous ARPES data which show topological surface state are also from this kind of samples (18). The samples used in the experiments were cleaved *in situ* and immediately transferred to a STM head. Experiments were performed in two different ultrahigh vacuum ( $1 \times 10^{-11}$  mbar) LT-STM systems, STM#1 (USM-1300s- $^3\text{He}$ ) and STM#2 (USM-1300- $^3\text{He}$  with a vector magnet), STM images were acquired in the constant-current mode with a tungsten tip. Differential conductance ( $dI/dV$ ) spectra were acquired by a standard lock-in amplifier at a frequency of 973.1 Hz, under modulation voltage  $V_{mod} = 0.1$  mV. The system energy resolution were calibrated on a clean Nb(111) surface prepared by repeated cycles of sputtering with argon ions and annealing at 1200 °C. Low temperatures of 0.4 K (0 T) and 0.55 K (4 T) are achieved by a single-shot  $^3\text{He}$  cryostat. A perpendicular magnetic field up to 11 Tesla for STM#1 and a vector magnetic field with the maximum value  $9_z-2_x-2_y$  Tesla for STM#2 can be applied to a sample surface. Data in part (II) & (III) of Fig. 3C, Figs. 3D and E, Figs. S2A-C and F-H, Figs. S3A-D, Figs. S4F and H (middle panels), Figs. S5-S6 were measured by STM#1, while others were from STM#2.

### I. Voltage offset and energy resolution calibrations

It is well known that the zero-bias offset problem exists in STM studies, and it is critically important in our study of the zero-energy peaks of MBS. We followed a standard procedure (40) in the field with extra cares. We calibrated the two STM systems with the standard method of overlap spot of  $I-V$  curves, since the current should be always zero when the voltage is zero. An example of this calibration is shown in Figs. S1 (A)-(B), which shows the zero-bias offset of 57.7  $\mu\text{eV}$ . This offset was then subtracted from all the following spectra under the same condition. We have recalibrated the STM several times during a cycle of measurement (usually in 17 hours) and found no detectable drift during the cycle. We have further confirmed this calibration by checking the particle-hole symmetry of the superconducting gap, as shown in Figs. S1 (C)-(D).

We calibrated the energy resolution by measuring a superconducting Nb single crystal. As shown in Fig. S1 (C), the overall broadening of the superconducting spectrum edge is about 0.3 meV for STM#1 and 0.26 meV for STM#2. By removing the temperature broadening term (0.12 meV for 0.4 K without applying a magnetic field), it shows that the energy resolution is better than 0.27 meV for STM#1 and 0.23 meV for STM#2 (41). The total broadening at 0.55 K is about 0.32 meV for STM#1 and 0.28 meV for STM#2.

$$\text{Total broadening} = \sqrt{r_{\text{Temperature}}^2 + r_{\text{System}}^2 + r_{\text{Scattering}}^2 + r_{\text{Others}}^2} \quad (\text{Eq. S1})$$

## II. Topological nontrivial and strong correlated properties of bulk bands

Fe(Te, Se) is a typical ‘11-type’ iron-based superconductor with the simplest crystal structure among all the iron-based superconductors. It has three hole-like bands around the  $\Gamma$  point and two electron-like bands around the M point in the bulk bands (23). Topological nontrivial band structure occurs around the  $\Gamma$ –Z high symmetric line when the  $p_z/d_{xy}$  anti-bonding orbital with an odd parity inverts with the  $d_{xz}/d_{yz}$  orbital which is even parity. This band inversion can be controlled by Te atom substitution. With increase of Te atoms, the interlayer  $p$ - $p$  orbital hybridization is strengthened while the intra-layer  $p_z$ - $d_{xy}$  hybridization is weakened. In addition, Te substitution also increases spin orbital coupling (SOC), which induces a gap opening at the band cross. Through this process, Fe(Te, Se) gains a nontrivial  $Z_2$  topological invariance, whose surface would have a topological surface state that has a helical spin structure (16), which has been clearly observed by a recent high-resolution spin-resolved ARPES experiment (18).

Fe(Te, Se) is also known to possess the strongest electron correlations among all the iron-based superconductors, with the mass renormalization of  $\sim 8$  for  $d_{xy}$  orbital and  $\sim 5$  for  $d_{xz}/d_{yz}$  orbitals (42 - 44). This heavily reduces the bandwidths and consequently the Fermi energies for all the bulk bands. An important consequence of small bulk Fermi energies is that the energy level spacing of Caroli-de Gennes-Matricon states inside the bulk vortex line, which is  $\Delta^2/E_F$ , is large enough (about 0.2 meV or larger, see Table S1) to allow a clear detection of MBSs at the low temperature (0.55 K) used in our experiment.

## III. Discussions on several trivial explanations of the observed zero-bias peak

A zero-bias conductance peak robust against perturbations is a necessary piece of evidence for a Majorana bound state in materials, which gives rise to resonant Andreev tunneling at the zero energy (45). Following theoretical proposals, zero-bias conductance peak has recently been observed in semiconductor nanowire devices (11, 14, 38, 46, 47) and ferromagnetic atomic chains (12, 48, 49). However, the energy gap separating the zero-energy MBS and excited quasiparticle states, which is required for the topological protection of MBS, is yet to be clearly demonstrated in both systems. Moreover, spatial profile of MBS in nanowires has not been measured. In the vortex version, a 2D surface provides a good platform not only to measure the pronounced zero-bias peak, but also to check detailed the spatial structure of Majorana wave function, that is, the spatial profile of zero-bias peak (5, 25).

It has been pointed out that several effects may cause a zero-bias peak in tunneling experiments, such as weak antilocalization (50, 51), reflectionless tunneling (52), Kondo effect (53, 54), Josephson supercurrent (55, 56) and packed CBS states near the zero energy (19, 20, 57, 58). Many of these alternative effects, such as reflectionless tunneling, involve Andreev reflection process between a normal lead and a disordered superconductor (59). However, Andreev process is significantly suppressed at the center of a vortex where the amplitude of the superconducting is forced to vanish (60). Other trivial explanations, as discussed in details below, are contradicted with our experiment observations.

1) *Reflectionless tunneling* is due to electron/hole phase conjugation through multiple Andreev reflection process, in which scattering centers make mirror-reflected electrons shoot back to the sample again. This effect can be ruled out by a relatively high magnetic field used

in our STM experiments as the extra phase accumulation induced by the magnetic field would destroy the phase conjugation condition. In the meanwhile, the vacuum tunneling configuration of STM does not benefit such a re-incident process, and the suppression of Andreev process on the vortex center also frustrates this effect.

2) *Kondo effect* can be ruled out by the zero field measurement shown in Figs. S4E & S4G, since there are no visible impurities in the areas selected for vortex measurement. Instead, our measurement shows a hard superconducting gap. In addition, sharp ZBPs appear over a large range of magnetic field as shown in Figs. S4F & S4H, which contradicts with the splitting of Kondo resonance peaks at high magnetic field (61).

3) *Josephson supercurrent* will manifest itself as a zero-bias peak in a conductance spectrum under a small tunneling barrier. However, the tungsten tip used in our experiment retains metallic at low temperature, and without containment from the superconducting sample, so there is no SIS junction that is required in Josephson tunneling. In addition, the zero-bias peak can be detected under a large tunneling barrier, which further rules out this explanation.

4) *Weak anti-localization (localization) effect* can cause a zero-bias conductance peak (dip) in the quantum diffusive transport region, where a phase destructive (constructive) interference of backscattered electrons is protected by the time reversal symmetry. Conventional weak anti-localization (WAL) was widely studied in topological insulators (62). This effect can be ruled out by the high magnetic field used in our experiment. But the Andreev process could provide a different mechanism for phase conjugation, no matter the time reversal symmetry holds or not. WAL can coexist with a magnetic field when tunneling from a normal lead to a superconductor. However, as we mentioned above, the condition for this effect is not satisfied in our measurements since the pairing strength must be zero at the vortex center and the Andreev process is strongly suppressed (63).

5) *Near-zero-energy packed CBS states* are common in vortices of conventional superconductors. However, as discussed in the main text and in this SI below, this scenario is inconsistent with our observations. First, CBS states inside a vortex core would shift toward the gap edge when moving from the core center to the edge of a vortex. They usually show dispersing features in a spatial line-cut plot as shown in Fig. S3C. It is not consistent with the non-split nature of ZBP we observed. Second, the energy of the lowest CBS is determined by the ratio of  $\Delta^2/E_F$ , which in our work is considerably large (about 0.7 meV for the surface band and greater than 0.2 meV for the bulk bands). That pushes the CBS away from the zero energy, exactly as we observed in Fig. S3E. Moreover, FWHM of the ZBP observed at low temperature is very sharp, thus the ZBP is unlikely an envelope peak formed by many CBS peaks near the zero energy.

We thus conclude that the above alternative effects cannot explain the ZBP observed in our measurements. Therefore, the most likely mechanism of the ZBP is Majorana quasiparticles enhanced resonant Andreev reflection (45), as one takes a comprehensive consideration regarding its spatial non-split line shape and its behaviors under different temperatures, magnetic fields, and tunneling barriers.

#### IV. Intrinsic inhomogeneity and different types of bound state inside vortex core

Figure S3 lists three different cases of bound states we observed inside vortex cores: 1) In some areas with no visible Fe or other impurities, strong MBS are observed inside vortex cores, CBS states is either absent or weak in this case, as shown in Fig. S2 and Figs. S3A & B. 2) In some areas, only CBS can be found inside a vortex core, as shown in Figs. S3 C, D. 3) There are also cases of coexistence of MBS and CBS, and CBS stays slightly away (usually around 0.2 - 0.7 meV) from the Fermi level at the center of the vortex core and disperses to the higher energy when moving away from the core center, while MBS always stays at the zero energy as shown in Figs. S3 E - H and Fig. S4F. This is consistent with the fact that the energy level spacing of CBS is controlled by  $\Delta^2/E_F$ , which has a value around 0.7 meV for the topological surface state and a minimal value of 0.2 meV for the bulk bands. In fact, the non-zero peak observed at the core center in Figs. S3E - H is at about 0.7 meV on the empty side, almost identical with the lowest CBS energy calculated with the extracted parameters of the Dirac surface bands in the main text ( $\Delta^2/E_F = 0.74$  meV). The fact that this CBS mode appears in the empty side also supports the origin of the electron-like surface Fermi surface since it is known that the lowest CBS peak appears only on empty (filled) state if the carriers are electron (hole) (64 - 66).

Statistically, we have about 20% success rate in observing isolated pure MBS during our more than 150 measurements, and our experience indicates the importance of high quality of single crystals and spatial homogeneity of superconducting gaps. While the exact reason of these variations is not fully understood yet, we offer two possible explanations below.

First, the bulk vortex line has low-lying sub-gap states. In the presence of disorder, the spectral gap inside the vortex line may close. The coupling of MBS to the zero-energy sub-gap states on the vortex line makes it move deeper beneath the surface and consequently reduces the tunneling conductance in STS, which is highly surface sensitive. Nonetheless, provided that the zero-energy states along the vortex line are localized, the MBS at the two ends remain spatially separated, and topologically protected. It may be also possible that disorder is sufficiently strong that drive a topological phase transition for the entire vortex line as suggested by Ref. (35), leading to ZBPs in some of the vortex cores while absent in others.

Second, since Te substitution plays a critical role on the topological nature of Fe(Te, Se), the inhomogeneous distribution of Te/Se, as observed by a previous TEM report (67) and our STM (see Fig. 1D), may introduce some non-topological regions in the bulk, thus causing disappearance of topological surface state and consequently MBS on some regions on the surface. In addition, the inhomogeneities of Te/Se substitution and charge doping due to charge transfer effect between chalcogen atoms and iron atoms (67) may also modify band dispersions and Fermi energies of both the bulk and surface states, which may affect the condition for detecting a Majorana mode in tunneling spectroscopy.

#### V. Non-split zero-bias peak under different magnetic field

Our field-dependent STM experiments reveal that the ZBP starts to emerge at 0.15 T, maintaining its zero-energy position up to 6.0 T, as shown in Fig. S4. With increasing the magnetic field, the inter-vortex length decreases, with the values of 70 nm, 32 nm, 25 nm and 20 nm at 0.5 T, 2.5 T, 4.0 T and 6.0 T, respectively. The amplitude and width of MBSs are

quite stable from 0.15 T to 6.0 T, indicating the ZBP in Fe(Te, Se) is very robust against the magnetic field. The relevant small coherence length of MBS shown in the main text enables MBS to be stable at sufficiently high magnetic field. The presence of ZBP and its non-split line profile exclude the possibilities that ZBPs made by Kondo resonance.

During our experiment, we carefully checked the selected area by a zero-field mapping before detailed vortex study. We make sure that there is no visible impurity state involved in the signal of zero bias peaks.

## VI. Additional results of temperature evolution

Typical ZBC maps under different temperatures are shown in Figs. S5A-S5D. At low temperature, vortices are more regular and show a strong conductance on the center. A low temperature line-cut intensity plot and a corresponding waterfall plot are shown in Figs. S5E and S5F, respectively. It is similar to the line-cuts shown in the main text and Fig. S2 that a spatial non-split pronounced ZBP dominates in a vortex core. At higher temperatures, the vortex becomes more irregular and diffusive. In addition, the conductance intensity at the vortex core decreases rapidly at high temperature. A high temperature line-cut intensity plot and a corresponding waterfall plot for the same vortex core are shown in Figs. S5G and S5H, respectively, showing disappearance of a ZBP.

Beyond what has been shown in Fig. 3 of the main text, two more cases of temperature evolution of MBS are shown in Figs. S6A and B, showing similar behaviors as the data in Fig. 3D. By measuring the normalized differential conductance differences between peak and valley, we summarize their temperature dependence for the two cases in Fig. S6C. It can be derived from Eq. S2 in the next part of SI that the conductance difference can be fitted by  $C/T$ .  $C$  is the fitting parameter and represent a characteristic temperature indicating the robustness of ZBP against thermal influence. Such the fits are shown in the left panel of Fig. S6C. As shown in right panel of Fig. S6C, it is evident that  $C$  is positively correlated with the low temperature amplitude of ZBP.

This temperature behavior of MBS can be understood in the following way, as schematically illustrated in Fig. S6D, at sufficient low temperature when the thermal energy is smaller than the energy level spacing of CBS inside the bulk vortex line, MBS at the end of vortex line can survive poisoning from thermal excited quasiparticles, as illustrated in the left panel of Fig. S6D. However, at higher temperature when the thermal energy is larger than the level spacing, MBS will be strongly poisoned by the thermally excited quasiparticles, as illustrated in the upper right panel of Fig. S6D. A simple quantitative analysis can estimate the value of MBS vanishing temperature. As shown in Table S1, the minimal value of the energy level spacing of CBS that is closely related to  $\Delta^2/E_F$  of the bulk which has a typical value of about 0.3 meV, compatible to the thermal energy ( $k_B T$ ) around 3 K. As shown in Fig. S6C, the extracted  $C$  parameter is different from vortex to vortex. It can be understood in the same scenario. As we mentioned in part IV of SI, the intrinsic spatial inhomogeneity of Fe(Te, Se) may allow different types of vortex line exist at different positions.

## VII. Additional results of tunneling barrier evolution

Tunneling barrier dependence data are measured within a fixed ‘setpoint’ voltage ( $V_s = -5$  mV). Different tunneling barriers are achieved by changing the tunneling current ( $I_t$ ), corresponding to changing of tip/sample spacing, while STM regulation loop is active. As mentioned in the main text, the tunneling barrier is parameterized by the conductance calculated by the STM ‘setpoint’ settings, that  $G_N \equiv I_t/V_s$ .  $G_N$  is an averaged normal state conductance which represents the conductance of tunneling barrier (68), which is more accurate than the high-bias conductance used in some studies on nanowire devices (38).

Majorana bound states can be observed in tunneling spectrum by resonant Andreev reflection coupled to a normal lead. It intrinsically leads to  $2e^2/h$  quantized conductance plateau at zero temperature. Under the conditions of finite temperature and large tunneling barrier, it is difficult to realize  $2e^2/h$  by STM configuration. A theoretical model based on resonant tunneling to a single Majorana mode (69) shows at low temperature ( $k_B T \ll \Delta_0$ ) and weak tunneling ( $\Gamma \ll \Delta_0$ ) conditions, the zero-bias conductance of a MBS can be scaled onto a simple function (Eq. S2), which only depends on a dimensionless ratio  $k_B T/\Gamma$  (30, 38), as shown in the inset of Fig. S7A.  $\Gamma$  is the parameter of tunneling broadening, which is the HWHM of a theoretical MBS at 0 K.

$$G_s = \frac{2e^2}{h} \int_{-\infty}^{+\infty} dE \frac{\Gamma^2}{E^2 + \Gamma^2} \frac{1}{4k_B T \cosh^2(E/2k_B T)} \quad (\text{Eq.S2})$$

$$= \frac{2e^2}{h} f(k_B T / \Gamma)$$

This scaling function gives the value of MBS conductance at a finite temperature with different tunneling barriers. That creates possibilities for us to verify the Majorana nature of the observed zero-bias peak below the quantized conductance region. We tried this strategy in Fig. S7A, where 49 zero-bias conductance of the ZBPs measured at 0.55 K are scaled and compared to the theoretical curve. We note that the relation  $\Gamma = \kappa G_N / (2e^2/h)$  holds at the sufficiently weak tunneling condition (30), and we choose the value  $\kappa = 170$  as a single adjustable parameter in the scaling process. We find the tunneling broadening in our experiment  $G_N$  interval is 2~4 orders of magnitude smaller than the FWHM of MBS (Fig. S7B). It is the reason of MBS width barely changes over two orders of magnitude in  $G_N$ .

Even the experimental data show the scaling behavior consistent very well with the theoretical curve, we cannot regard this result as a supporting evidence of Majorana bound states. All of data point shown in Fig. S7A are measured in the weak coupling region in which the linear scaling behavior of STM itself can also lead to this good consistence. It will be more convincing to try this strategy under the condition of lower temperature and lower tunneling barrier (small  $k_B T/\Gamma$ ), which push the experiment beyond the linear region of scaling function.

Tunneling barrier dependence measurement is repeated on another vortex (Figs. S7C & D), in which we obtain a similar behavior.

### VIII. Details of MBS wave function calculation

Details of MBS wave function calculations are as follows. From previous theoretical work (5,25), the intensity of Majorana wave function can be written as

$$|u|^2 = |f(r)|^2 + |g(r)|^2 \quad (\text{Eq.S3})$$

Where

$$\begin{aligned} f(r) &= J_0\left(\frac{E_F r}{v_F}\right) \exp\left[-\int^r \frac{\Delta(r')}{v_F} dr'\right] (i+1) \\ g(r) &= J_1\left(\frac{E_F r}{v_F}\right) \exp\left[-\int^r \frac{\Delta(r')}{v_F} dr'\right] (i-1) \end{aligned} \quad (\text{Eq.S4})$$

We use a step function of  $\Delta(r)$  ( $\Delta = 1.8$  meV ( $r > 8$  nm);  $\Delta = 0$  meV ( $r < 8$  nm)) in the equation and derive the  $|u|^2$

$$|u|^2 = C \sum_{i=0}^1 \left[ J_i\left(\frac{E_F r}{\Delta_0 \xi_0}\right) e^{-\frac{(r-80)}{\xi_0}} \right]^2 \quad (\text{Eq.S5})$$

where  $J_i(x)$  is the Bessel function,  $\Delta(r)$  is the superconducting pairing potential,  $E_F$  is the Fermi energy,  $v_F$  is the Fermi velocity,  $\Delta_0$  and  $\xi_0$  are the superconducting gap and the coherence length at zero temperature, respectively. At temperatures higher than the level broadening of Majorana mode, the tunneling current is proportional to  $|u|^2$ .

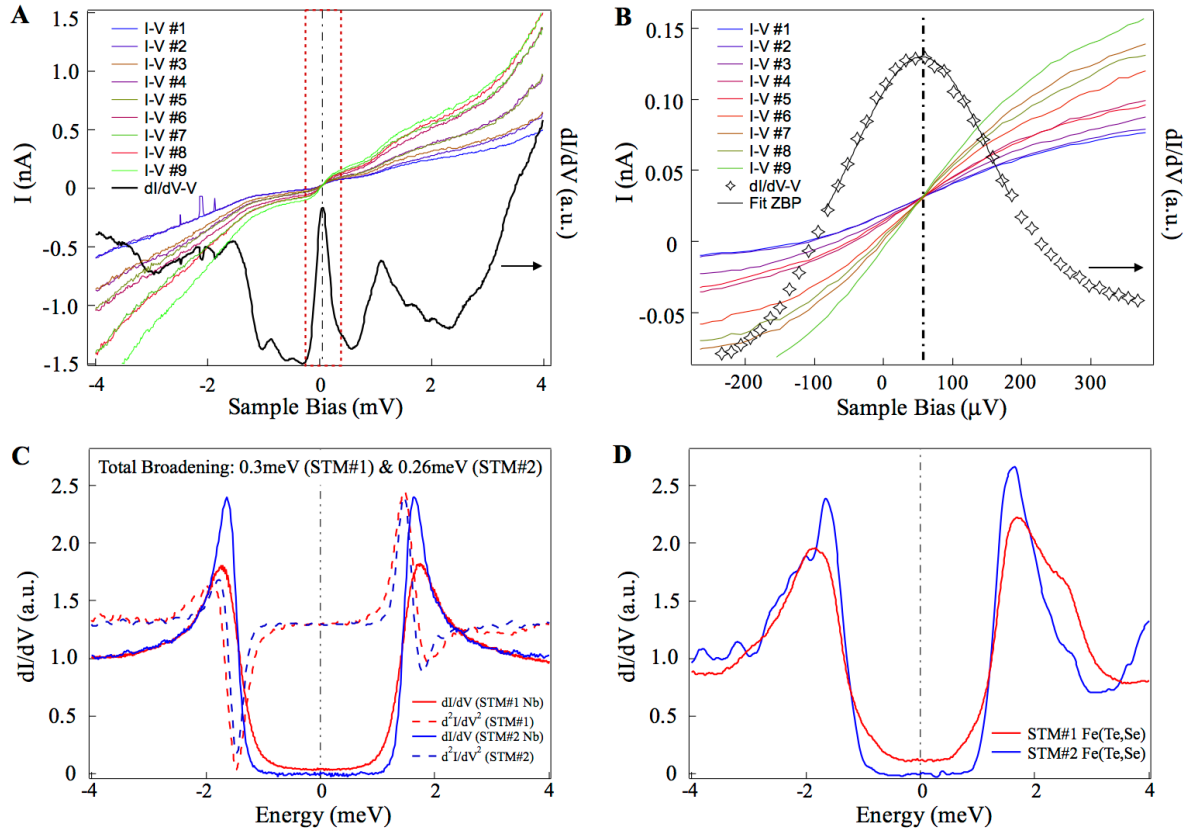


**Fig. S1. Voltage offset and energy resolution calibrations.** (A)-(B) Raw STS data before voltage offset calibration. (A) Simultaneous spectra measured at a vortex core center. There are 9  $I-V$  curves with different values of tunneling resistance, the overlapping point which has a true zero current should have a true zero voltage. The  $dI/dV$  curves, obtained from lock-in techniques simultaneously, showing its peak position exactly at this overlapping point. (B) A zoom-in plot of the red dash box in A, showing that this particular voltage offset is  $57.7 \mu\text{eV}$ . The energy step of the  $dI/dV$  curve is  $14 \mu\text{eV}$ . (C)-(D) Superconducting spectra after their voltage offset calibrations measured by two LT-STM systems, showing the particle-hole symmetry of the superconducting gap. (C) Superconducting gap of a Nb single crystal measured at  $0.4 \text{ K} / 0 \text{ T}$ . The total broadening of the superconducting gap edge is  $0.3 \text{ meV}$  for STM#1 and  $0.26 \text{ meV}$  for STM#2. (D) Superconducting gap of FeTe<sub>0.55</sub>Se<sub>0.45</sub> single crystals measured at  $0.4 \text{ K} / 0 \text{ T}$  which can form a MBS inside a vortex core under the magnetic field.

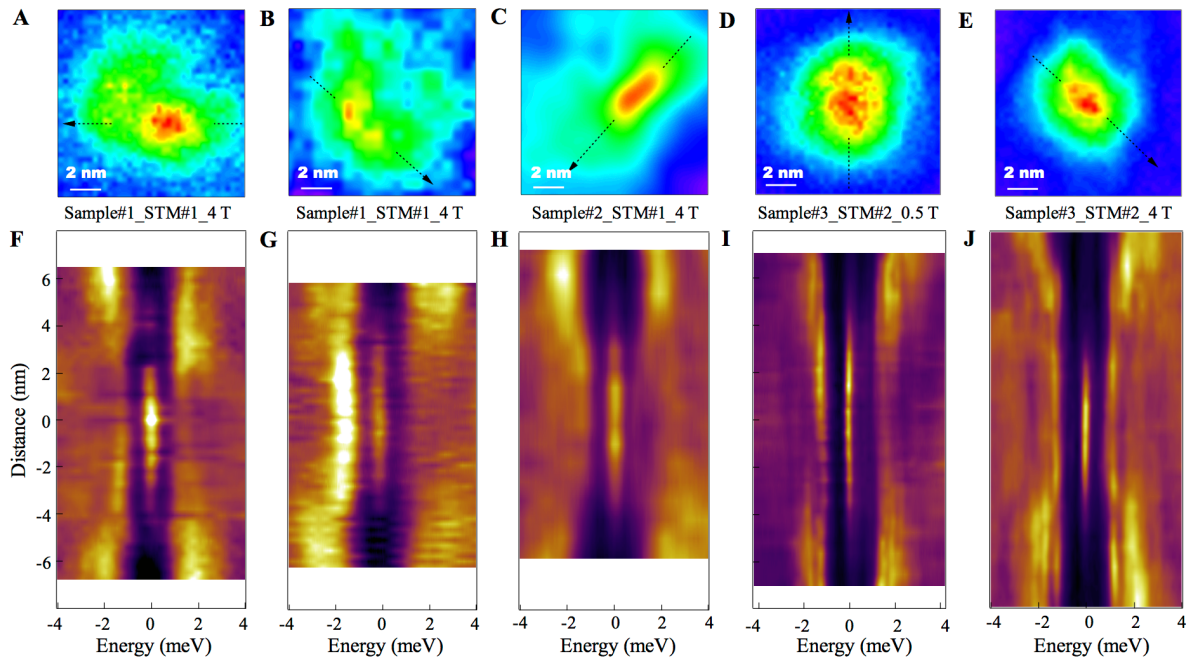


**Fig. S2. Spatial line profile reproducibility under different samples, magnetic fields, and equipment.** (A)-(E) ZBC maps (area = 12 nm × 12 nm) around vortex cores. (F)-(J) line-cut intensity plots along the black dash line indicated in (A)-(E), respectively. The data are normalized by integrated area of each  $dI/dV$  spectrum.

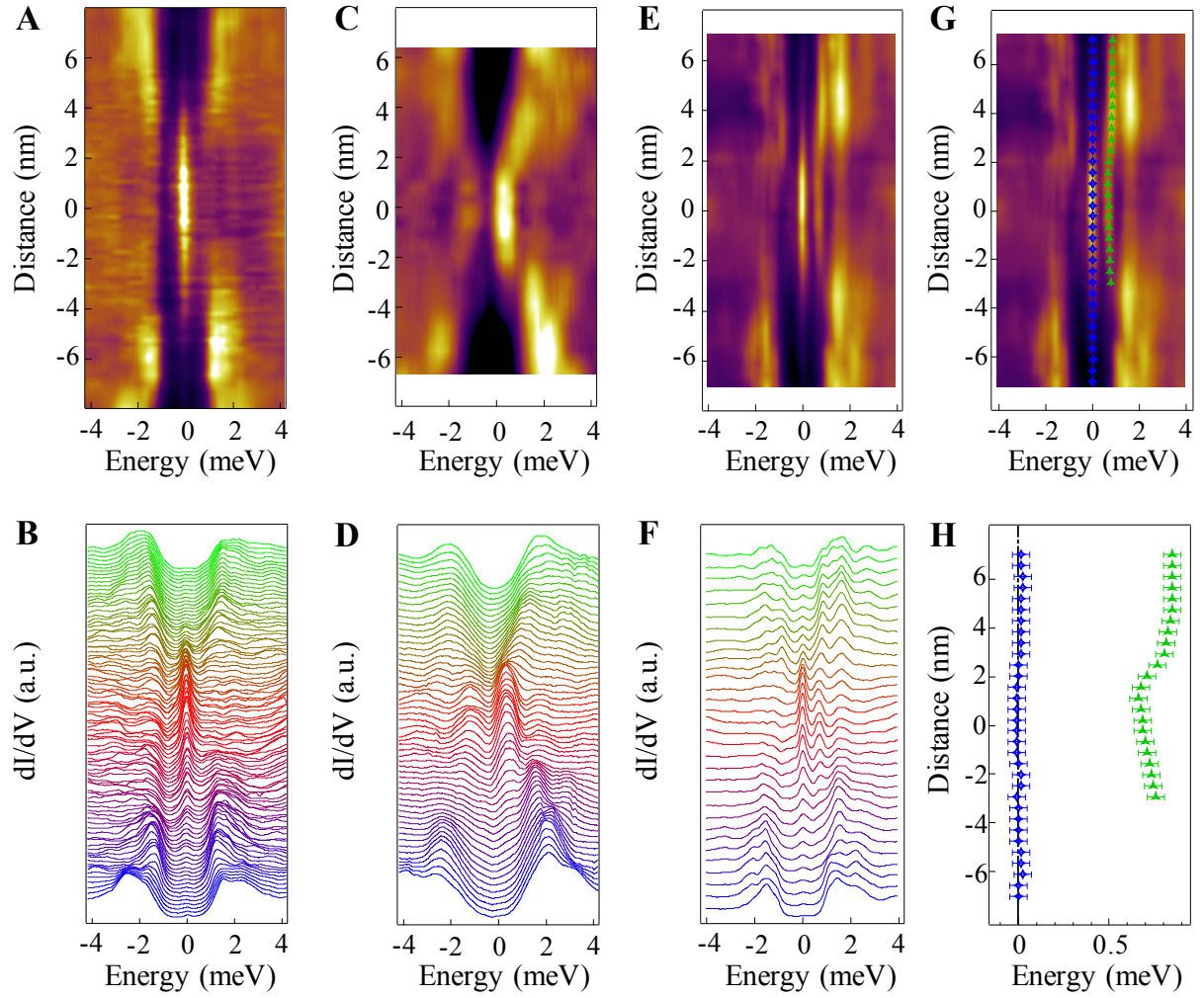


**Fig. S3. Three types of bound states inside vortex cores of  $\text{FeTe}_{0.55}\text{Se}_{0.45}$ .** (A)-(B) Line-cut and waterfall plots of pure Majorana bound states (4 T). (C)-(D) Line-cut and waterfall plots of CBS. In this case no zero-bias peaks were observed (4 T). (E)-(F) Line-cut and waterfall plots of co-existence cases. Both non-dispersive MBS peaks and dispersive CBS peaks ( $\sim 0.7$  meV) were observed (6 T). (G) Overlapping display of extracted peak positions and line-cut plots of the co-existence case. (H) Extracted peak positions of the co-existence case. All the data were measured at 0.55 K.

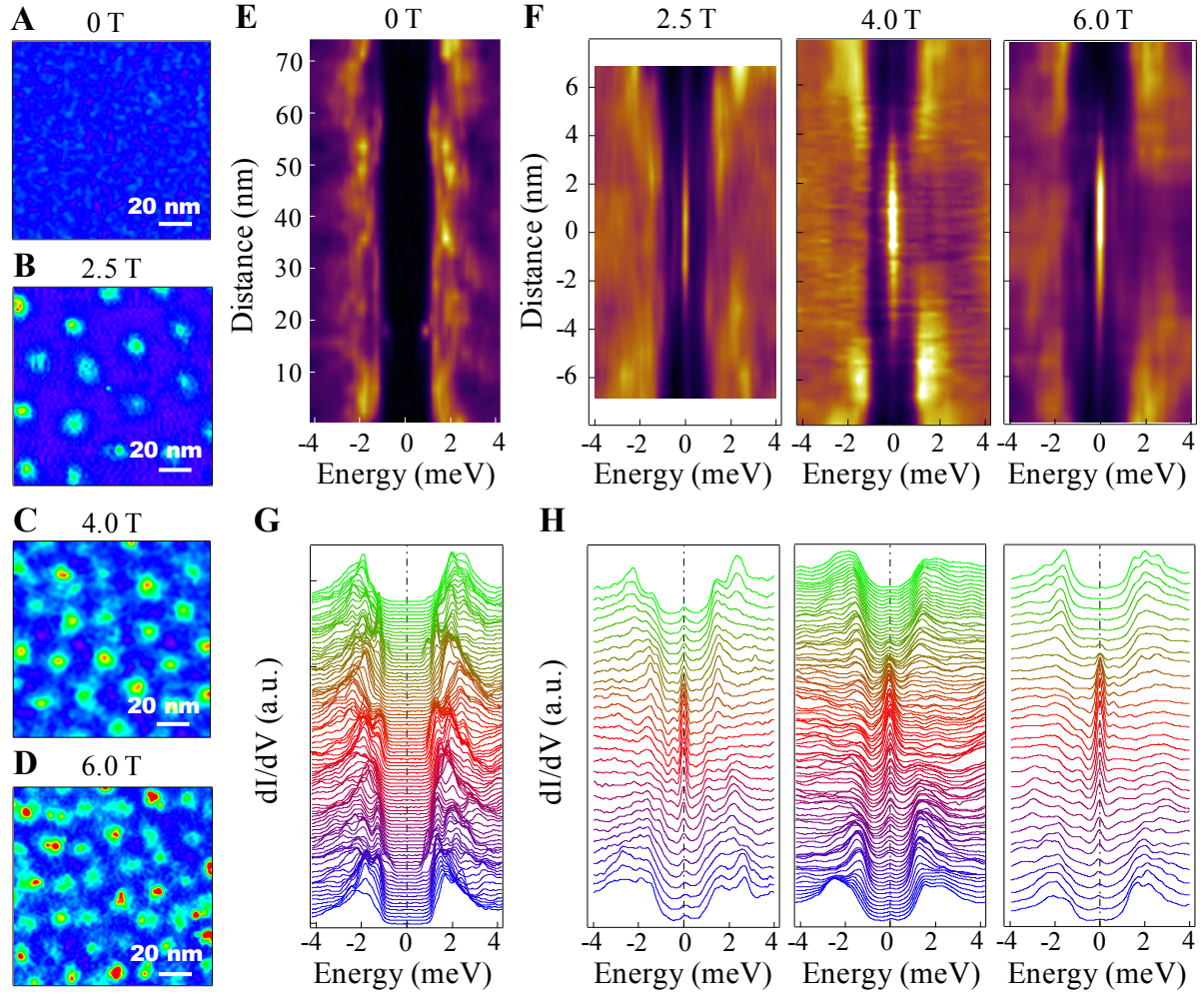


**Fig. S4. Majorana bound states under different magnetic fields.** (A)-(D)  $120 \text{ nm} \times 120 \text{ nm}$  ZBC maps at different magnetic fields. Inter-vortex length decreases with increasing magnetic field, that is, 70 nm for 0.5 T (Fig. 1E), 32 nm for 2.5 T, 25 nm for 4.0 T, and 20 nm for 6.0 T. They are consistent with theoretical prediction on Abrikosov vortex lattice, that is, 68 nm for 0.5 T, 30 nm for 2.5 T, 24 nm for 4.0 T, and 19.6 nm for 6.0 T. (E)-(F) Line-cut intensity plots at 0 T, 2.5 T, 4.0 T, and 6.0 T respectively. (G)-(H) Corresponding waterfall plot at 0 T, 2.5 T, 4.0 T, and 6.0 T. Zero magnetic field spectra show full superconducting gap and spatial inhomogeneity of  $\text{FeTe}_{0.55}\text{Se}_{0.45}$ . Note that a weak CBS coexists with the MBS at data of 2.5 T (6.0 T). The CBS peak locates at about  $-0.5 \text{ meV}$  ( $+0.6 \text{ meV}$ ) in the core center and disperses toward the gap edge away from the core center. Settings: 4.0 T data measured by STM#1 with settings,  $V_s = -10 \text{ mV}$ ,  $I_t = 100 \text{ pA}$ , and  $T = 0.55 \text{ K}$ , while other data are measured by STM#2 with  $V_s = -5 \text{ mV}$ ,  $I_t = 200 \text{ pA}$ .

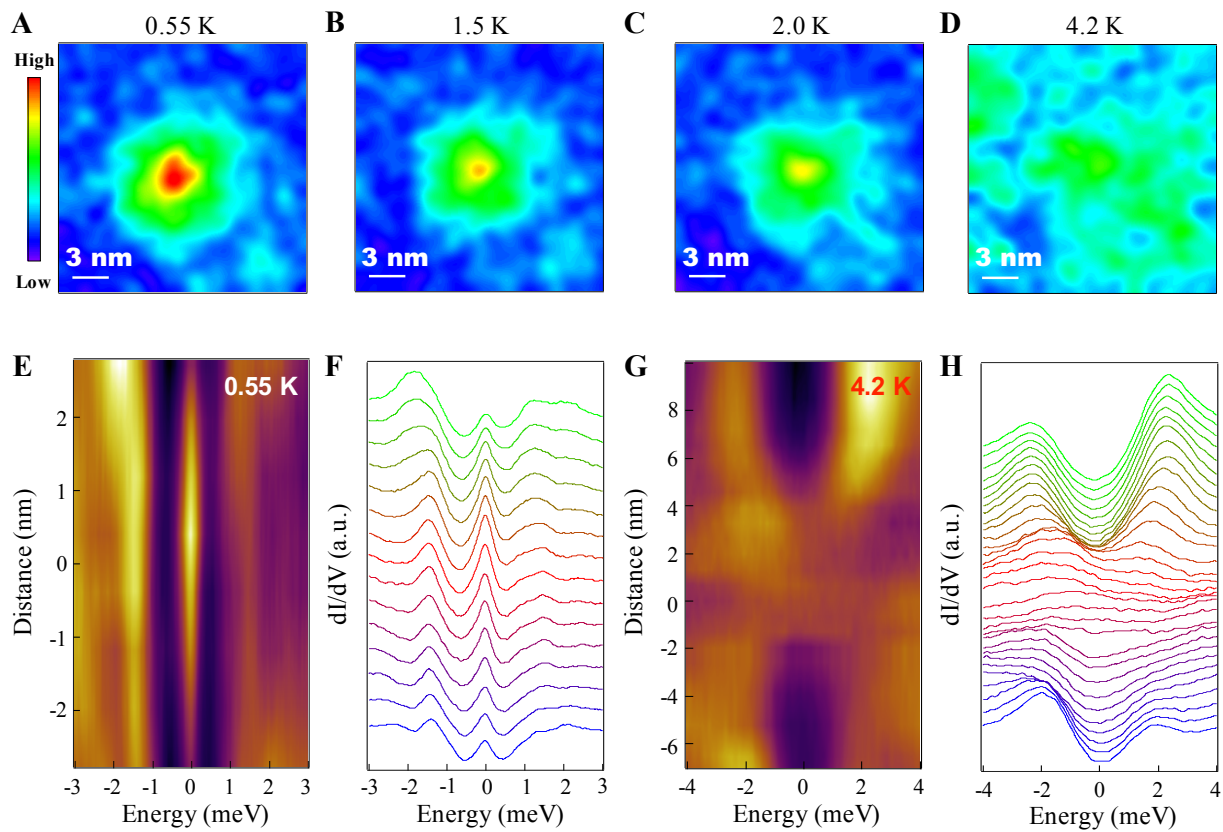


**Fig. S5. Line profile under low and high temperature.** (A)-(D) ZBC map at 0.55 K, 1.5 K, 2.0 K, and 4.2 K respectively. (E) Typical low temperature line profile at 0.55 K. (F) Waterfall plot of (E). (G) Typical higher temperature line profile at 4.2 K. (H) Waterfall plot of (G). All the data were measured at 4.0 T.

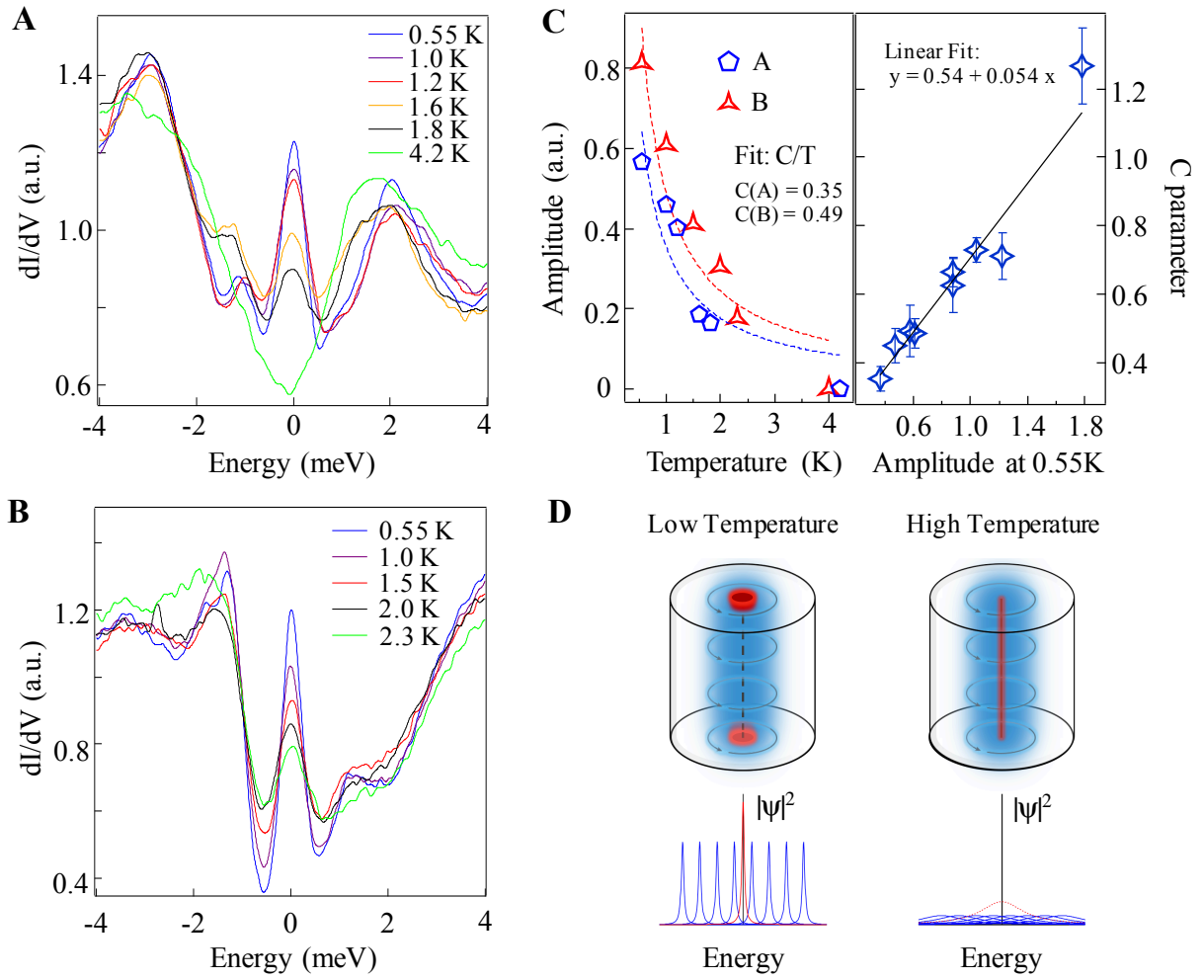


**Fig. S6. More examples of MBS temperature evolution.** (A)-(B) Two examples of Majorana ZBPs at the center of vortex core under different temperatures. (C) Left panel:  $C/T$  fitting of amplitude of Majorana ZBPs under different temperatures. Blue hexagons are extracted from spectra in Fig. S6A. Red triangles are extracted from spectra in Fig. S6B. Right panel: summary on several temperature evolution measurements. The fitting parameter  $C$ , a characteristic temperature indicating MBS robustness against thermal influence, is positively correlated with the ZBP amplitude measured at 0.55 K. This indicates stronger Majorana ZBPs can survive at higher temperature. (D) Schematic explanation of the temperature effect on Majorana ZBPs. Upper row: schematic of a vortex with a vertical magnetic field applied at low and high temperature. Lower row: corresponding schematic of the energy-resolved bound states inside the vortex line (Red solid curves: Majorana ZBPs at the ends of the vortex line; blue curves: CBSs inside the bulk vortex line. All data sets are measured under 4 T and  $I_t = 100$  pA,  $V_s = -10$  mV. (Tunneling barrier conductance:  $G_N \equiv I_t / V_s = 1.29 \times 10^{-4} \times 2e^2/h$ )

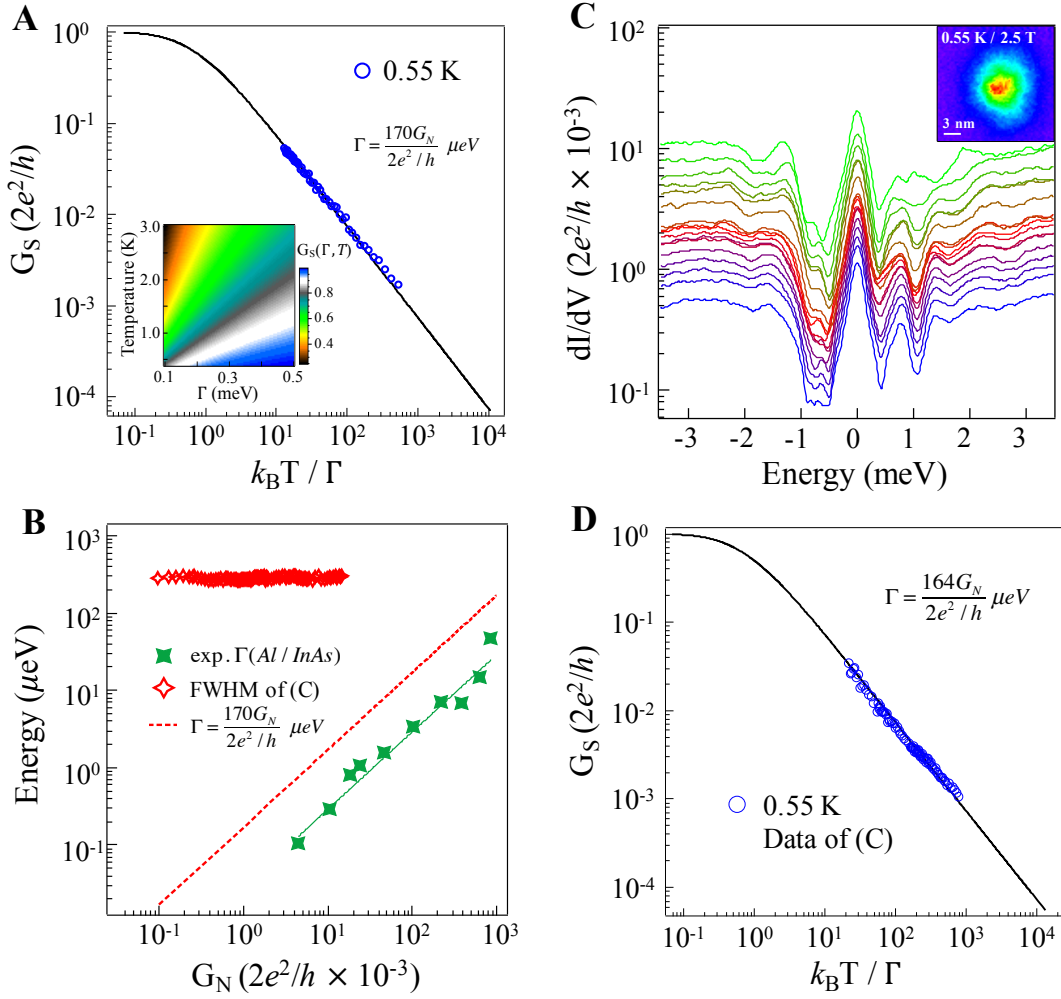


**Fig. S7. Additional Results of tunneling barrier evolution.** (A) Scaling behavior of the zero-bias conductance (ZBC) shown in Fig. 3A of the main text. Black line: Calculated ZBC of a single Majorana mode at low temperature using Eq. S2; Blue circles: ZBC of spectra at 0.55 K. Inset figure: calculation plot of  $G_S(\Gamma, T)$ . (B) Red dash line is a plot of tunneling broadening following the formula inset. Red stars are FWHM of spectra in (C). The average value of FWHM is about 0.28 meV. Green stars are tunneling broadening in nanowire devices. It is extracted from Fig. 3A in Ref. 38. (C) Another set of data about tunneling barrier evolution of MBS measured at 0.55 K and 2.5 T. MBSs locate at zero energy over two orders of magnitude in tunneling barrier conductance. Inset figure: ZBC map. (D) Scaling behavior of the ZBC shown in Fig. S7C.

**Table S1. Band Parameters of Fe(Te, Se)**

Orbital/Band	$\Delta$ (meV)	$E_F$ (meV)	$\Delta^2/E_F$ (meV)
$\Gamma$ (TSS)	1.8	4.4	0.74
$\Gamma$	2.5	5~30	0.21~1.25
M	4.2	15~40	0.44~1.18

## Reference:

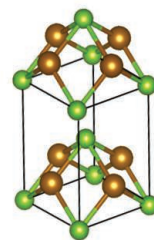
1. A. Y. Kitaev, Fault-tolerant quantum computation by anyons. *Ann. Phys.* **303**, 2-30 (2003). [doi:10.1016/S0003-4916\(02\)00018-0](https://doi.org/10.1016/S0003-4916(02)00018-0)
2. C. Nayak, S. H. Simon, A. Stern, M. Freedman, and S. Das Sarma, Non-Abelian anyons and topological quantum computation. *Rev. Mod. Phys.* **80**, 1083-1159 (2008). [doi:10.1103/RevModPhys.80.1083](https://doi.org/10.1103/RevModPhys.80.1083)
3. A. Y. Kitaev, Unpaired Majorana fermions in quantum wires. *Physics-Uspokhi* **44**, 131–136 (2001). [doi:10.1070/1063-7869/44/10S/S29N](https://doi.org/10.1070/1063-7869/44/10S/S29N).
4. N. Read, D. Green, Paired states of fermions in two dimensions with breaking of parity and time-reversal symmetries and the fractional quantum Hall effect. *Phys. Rev. B* **61**, 10267–10297 (2000). [doi:10.1103/PhysRevB.61.10267](https://doi.org/10.1103/PhysRevB.61.10267)
5. L. Fu, C. L. Kane, Superconducting proximity effect and majorana fermions at the surface of a topological insulator. *Phys. Rev. Lett.* **100**, 096407 (2008). [Medline](https://pubmed.ncbi.nlm.nih.gov/16811111/) [doi:10.1103/PhysRevLett.100.096407](https://doi.org/10.1103/PhysRevLett.100.096407)
6. R. M. Lutchyn, J. D. Sau, S. Das Sarma, Majorana fermions and a topological phase transition in semiconductor-superconductor heterostructures. *Phys. Rev. Lett.* **105**, 077001 (2010). [Medline](https://pubmed.ncbi.nlm.nih.gov/19811111/) [doi:10.1103/PhysRevLett.105.077001](https://doi.org/10.1103/PhysRevLett.105.077001)
7. Y. Oreg, G. Refael, F. von Oppen, Helical liquids and Majorana bound states in quantum wires. *Phys. Rev. Lett.* **105**, 177002 (2010). [Medline](https://pubmed.ncbi.nlm.nih.gov/19811111/) [doi:10.1103/PhysRevLett.105.177002](https://doi.org/10.1103/PhysRevLett.105.177002)
8. Andrew C. Potter and Patrick A. Lee, Multichannel generalization of Kitaev's Majorana end states and a practical route to realize them in thin films. *Phys. Rev. Lett.* **105**, 227003 (2010) [doi:10.1103/PhysRevLett.105.227003](https://doi.org/10.1103/PhysRevLett.105.227003)
9. X.-L. Qi, Taylor L. Hughes, and S.-C. Zhang, Chiral topological superconductor from the quantum Hall state. *Phys. Rev. B* **82**, 184516 (2010) [doi:10.1103/PhysRevB.82.184516](https://doi.org/10.1103/PhysRevB.82.184516)
10. S. Nadj-Perge, I. K. Drozdov, B. A. Bernevig, A. Yazdani, Proposal for realizing Majorana fermions in chains of magnetic atoms on a superconductor. *Phys. Rev. B* **88**, 020407 (2013). [doi:10.1103/PhysRevB.88.020407](https://doi.org/10.1103/PhysRevB.88.020407)
11. V. Mourik, K. Zuo, S. M. Frolov, S. R. Plissard, E. P. Bakkers, L. P. Kouwenhoven, Signatures of Majorana fermions in hybrid superconductor-semiconductor nanowire devices. *Science* **336**, 1003–1007 (2012). [Medline](https://pubmed.ncbi.nlm.nih.gov/2223360/) [doi:10.1126/science.1222360](https://doi.org/10.1126/science.1222360)
12. S. Nadj-Perge, I. K. Drozdov, J. Li, H. Chen, S. Jeon, J. Seo, A. H. MacDonald, B. A. Bernevig, A. Yazdani, Observation of Majorana fermions in ferromagnetic atomic chains on a superconductor. *Science* **346**, 602–607 (2014). [doi:10.1126/science.1259327](https://doi.org/10.1126/science.1259327) [Medline](https://pubmed.ncbi.nlm.nih.gov/259327/)
13. H. H. Sun, K.-W. Zhang, L.-H. Hu, C. Li, G.-Y. Wang, H.-Y. Ma, Z.-A. Xu, C.-L. Gao, D.-D. Guan, Y.-Y. Li, C. Liu, D. Qian, Y. Zhou, L. Fu, S.-C. Li, F.-C. Zhang, J.-F. Jia, Majorana zero mode detected with spin selective Andreev reflection in the vortex of a topological superconductor. *Phys. Rev. Lett.* **116**, 257003 (2016). [doi:10.1103/PhysRevLett.116.257003](https://doi.org/10.1103/PhysRevLett.116.257003) [Medline](https://pubmed.ncbi.nlm.nih.gov/257003/)
14. M. T. Deng, S. Vaitiekėnas, E. B. Hansen, J. Danon, M. Leijnse, K. Flensberg, J. Nygård, P. Krogstrup, C. M. Marcus, Majorana bound state in a coupled quantum-dot hybrid-nanowire system. *Science* **354**, 1557–1562 (2016). [doi:10.1126/science.aaf3961](https://doi.org/10.1126/science.aaf3961) [Medline](https://pubmed.ncbi.nlm.nih.gov/25961/)
15. Q. L. He, L. Pan, A. L. Stern, E. Burks, X. Che, G. Yin, J. Wang, B. Lian, Q. Zhou, E. S. Choi, K. Murata, X. Kou, T. Nie, Q. Shao, Y. Fan, S.-C. Zhang, K. Liu, J. Xia,

- K. L. Wang, Chiral Majorana edge state in a quantum anomalous hall insulator-superconductor structure, *Science* **357**, 294-299 (2017). [doi:10.1126/science.aag2792](https://doi.org/10.1126/science.aag2792)
16. Z. Wang, P. Zhang, G. Xu, L. K. Zeng, H. Miao, X. Xu, T. Qian, H. Weng, P. Richard, A. V. Fedorov, H. Ding, X. Dai, Z. Fang, Topological nature of the FeSe<sub>0.5</sub>Te<sub>0.5</sub> superconductor. *Phys. Rev. B* **92**, 115119 (2015). [doi:10.1103/PhysRevB.92.115119](https://doi.org/10.1103/PhysRevB.92.115119)
  17. X. Wu, S. Qin, Y. Liang, H. Fan, J. Hu, Topological characters in Fe(Te<sub>1-x</sub>Se<sub>x</sub>) thin films. *Phys. Rev. B* **93**, 115129 (2016). [doi:10.1103/PhysRevB.93.115129](https://doi.org/10.1103/PhysRevB.93.115129)
  18. P. Zhang, K. Yaji, T. Hashimoto, Y. Ota, T. Kondo, K. Okazaki, Z. Wang, J. Wen, G. D. Gu, H. Ding, and S. Shin, Observation of topological superconductivity on the surface of iron-based superconductor. *Science* **360**, 182-186 (2018). [doi:10.1126/science.aan4596](https://doi.org/10.1126/science.aan4596)
  19. C. Caroli, P. G. de Gennes, J. Matricon, Bound Fermion states on a vortex line in a type II superconductor. *Phys. Lett.* **9**, 307-309 (1964). [doi:10.1016/0031-9163\(64\)90375-0](https://doi.org/10.1016/0031-9163(64)90375-0)
  20. H. F. Hess, R. B. Robinson, J. V. Waszczak, Vortex-core structure observed with a scanning tunneling microscopy. *Phys. Rev. Lett.* **64**, 2711-2714 (1990). [doi:10.1103/PhysRevLett.64.2711](https://doi.org/10.1103/PhysRevLett.64.2711)
  21. T. Hanaguri, S. Niitaka, K. Kuroki, H. Takagi, Unconventional s-wave superconductivity in Fe(Se,Te). *Science* **328**, 474-476 (2010). [doi:10.1126/science.1187399](https://doi.org/10.1126/science.1187399) [Medline](#)
  22. F. Masee, P. O. Sprau, Y.-L. Wang, J. C. S. Davis, G. Ghigo, G. D. Gu, W.-K. Kwok, Imaging atomic-scale effects of high-energy ion irradiation on superconductivity and vortex pinning in Fe(Se,Te). *Sci. Adv.* **1**, e1500033 (2015). [doi:10.1126/sciadv.1500033](https://doi.org/10.1126/sciadv.1500033) [Medline](#)
  23. H. Miao, P. Richard, Y. Tanaka, K. Nakayama, T. Qian, K. Umezawa, T. Sato, Y.-M. Xu, Y. B. Shi, N. Xu, X.-P. Wang, P. Zhang, H.-B. Yang, Z.-J. Xu, J. S. Wen, G.-D. Gu, X. Dai, J.-P. Hu, T. Takahashi, H. Ding, Isotropic superconducting gaps with enhanced pairing on electron Fermi surfaces in FeTe<sub>0.55</sub>Se<sub>0.45</sub>. *Phys. Rev. B* **85**, 094506 (2012). [doi:10.1103/PhysRevB.85.094506](https://doi.org/10.1103/PhysRevB.85.094506)
  24. Supplementary materials
  25. Y. Wang and L. Fu, Topological phase transitions in multicomponent superconductors, *Phys. Rev. Lett.* **119**, 187003 (2017). [doi:10.1103/PhysRevLett.119.187003](https://doi.org/10.1103/PhysRevLett.119.187003)
  26. C. Chiu, M. Gilbert, T. Hughes, Vortex lines in topological insulator-superconductor heterostructures. *Phys. Rev. B* **84**, 144507 (2011). [doi:10.1103/PhysRevB.84.144507](https://doi.org/10.1103/PhysRevB.84.144507)
  27. L.-H. Hu, Ch. Li, D.-H. Xu, Y. Zhou, and F.-Ch. Zhang, Theory of spin-selective Andreev reflection in the vortex core of a topological superconductor, *Phys. Rev. B* **94**, 224501 (2016). [doi:10.1103/PhysRevB.94.224501](https://doi.org/10.1103/PhysRevB.94.224501)
  28. J.-P. Xu, C. Liu, M.-X. Wang, J. Ge, Z.-L. Liu, X. Yang, Y. Chen, Y. Liu, Z.-A. Xu, C.-L. Gao, D. Qian, F.-C. Zhang, J.-F. Jia, Artificial topological superconductor by the proximity effect. *Phys. Rev. Lett.* **112**, 217001 (2014). [doi:10.1103/PhysRevLett.112.217001](https://doi.org/10.1103/PhysRevLett.112.217001)
  29. J.-P. Xu, M.-X. Wang, Z. L. Liu, J.-F. Ge, X. Yang, C. Liu, Z. A. Xu, D. Guan, C. L. Gao, D. Qian, Y. Liu, Q.-H. Wang, F.-C. Zhang, Q.-K. Xue, J.-F. Jia, Experimental detection of a Majorana mode in the core of a magnetic vortex inside a topological insulator-superconductor Bi<sub>2</sub>Te<sub>3</sub>/NbSe<sub>2</sub> heterostructure. *Phys. Rev. Lett.* **114**, 017001 (2015). [doi:10.1103/PhysRevLett.114.017001](https://doi.org/10.1103/PhysRevLett.114.017001)

30. F. Setiawan, C.-X. Liu, J. D. Sau, and S. D. Sarma, Electron temperature and tunnel coupling dependence of zero-bias and almost-zero-bias conductance peaks in Majorana nanowires. *Phys. Rev. B* **96**, 184520 (2017). [doi:10.1103/PhysRevB.96.184520](https://doi.org/10.1103/PhysRevB.96.184520)
31. S. Das Sarma, Amit Nag, and Jay D. Sau, How to infer non-Abelian statistics and topological visibility from tunneling conductance properties of realistic Majorana nanowires. *Phys. Rev. B* **94**, 035143 (2016). [doi:10.1103/PhysRevB.94.035143](https://doi.org/10.1103/PhysRevB.94.035143)
32. Y. Yin, M. Zech, T. L. Williams, X. F. Wang, G. Wu, X. H. Chen, J. E. Hoffman, Scanning tunneling spectroscopy and vortex imaging in the iron pnictide superconductor  $\text{BaFe}_{1.8}\text{Co}_{0.2}\text{As}_2$ . *Phys. Rev. Lett.* **102**, 097002 (2009). [doi:10.1103/PhysRevLett.102.097002](https://doi.org/10.1103/PhysRevLett.102.097002)
33. C. Renner, A. D. Kent, P. Niedermann, Ø. Fischer, and F. Lévy, Scanning tunneling spectroscopy of a vortex core from the clean to the dirty limit. *Phys. Rev. Lett.* **67**, 1650 (1991). [doi: 10.1103/PhysRevLett.67.1650](https://doi.org/10.1103/PhysRevLett.67.1650)
34. J. Colbert and P. A. Lee, Proposal to measure the quasiparticle poisoning time of Majorana bound states. *Phys. Rev. B* **89**, 140505 (2014). [doi:10.1103/PhysRevB.89.140505](https://doi.org/10.1103/PhysRevB.89.140505)
35. P. Hosur, P. Ghaemi, R. S. K. Mong, A. Vishwanath, Majorana modes at the ends of superconductor vortices in doped topological insulators. *Phys. Rev. Lett.* **107**, 097001 (2011). [doi:10.1103/PhysRevLett.107.097001](https://doi.org/10.1103/PhysRevLett.107.097001)
36. H.-H. Hung, P. Ghaemi, T. L. Hughes, and M. J. Gilbert, Vortex lattices in the superconducting phases of doped topological insulators and heterostructures. *Phys. Rev. B* **87**, 035401 (2013). [doi: 10.1103/PhysRevB.87.035401](https://doi.org/10.1103/PhysRevB.87.035401)
37. G. Xu, B. Lian, P. Tang, X.-L. Qi, S.-C. Zhang, Topological superconductivity on the surface of Fe-based superconductors. *Phys. Rev. Lett.* **117**, 047001 (2016). [doi:10.1103/PhysRevLett.117.047001](https://doi.org/10.1103/PhysRevLett.117.047001) [Medline](#)
38. F. Nichele, A. C. C. Drachmann, A. M. Whiticar, E. C. T. O'Farrell, H. J. Suominen, A. Fornieri, T. Wang, G. C. Gardner, C. Thomas, A. T. Hatke, P. Krogstrup, M. J. Manfra, K. Flensberg, and C. M. Marcus, Scaling of Majorana Zero-Bias Conductance Peaks. *Phys. Rev. Lett.* **119**, 136803 (2017). [doi:10.1103/PhysRevLett.119.136803](https://doi.org/10.1103/PhysRevLett.119.136803)
39. J. Wen, G. Xu, Z. Xu, Z. W. Lin, Q. Li, W. Ratcliff, G. Gu, and J. M. Tranquada, Short-range incommensurate magnetic order near the superconducting phase boundary in  $\text{Fe}_{1+\delta}\text{Te}_{1-x}\text{Se}_x$ . *Phys. Rev. B* **80**, 104506 (2009). [doi:10.1103/PhysRevB.80.104506](https://doi.org/10.1103/PhysRevB.80.104506)
40. J.-X. Yin, Z. Wu, J.-H. Wang, Z.-Y. Ye, J. Gong, X.-Y. Hou, L. Shan, A. Li, X.-J. Liang, X.-X. Wu, J. Li, C.-S. Ting, Z.-Q. Wang, J.-P. Hu, P.-H. Hor, H. Ding, S. H. Pan, Observation of a robust zero-energy bound state in iron-based superconductor  $\text{Fe}(\text{Te},\text{Se})$ . *Nat. Phys.* **11**, 543–546 (2015). [doi:10.1038/nphys3371](https://doi.org/10.1038/nphys3371)
41. Y. J. Song, A. F. Otte, V. Shvarts, Z. Zhao, Y. Kuk, S. R. Blankenship, A. Band, F. M. Hess, and J. A. Stroscio, Invited Review Article: A 10 mK scanning probe microscopy facility. *Rev. Sci. Instrum.* **81**, 121101 (2010). [doi:10.1063/1.3520482](https://doi.org/10.1063/1.3520482)
42. Z. P. Yin, K. Haule, G. Kotliar, Spin dynamics and orbital-antiphase pairing symmetry in iron-based superconductors. *Nat. Phys.* **10**, 845–850 (2014). [doi:10.1038/nphys3116](https://doi.org/10.1038/nphys3116)
43. S. Rinott, K. B. Chashka, A. Ribak, E. D. L. Rienks, A. Taleb-Ibrahimi, P. L. Fevre, F. Bertran, M. Randeria, A. Kanigel, Tuning across the BCS-BEC crossover in the

- multiband superconductor  $\text{Fe}_{1+y}\text{Se}_x\text{Te}_{1-x}$ : An angle-resolved photoemission study. *Sci. Adv.* **3**, e1602372 (2017). [doi:10.1126/sciadv.1602372](https://doi.org/10.1126/sciadv.1602372)
44. Y. Lubashevsky, E. Lahoud, K. Chashka, D. Podolsky, A. Kanigel, Shallow pockets and very strong coupling superconductivity in  $\text{FeSe}_x\text{Te}_{1-x}$ . *Nat. Phys.* **8**, 309–312 (2012). [doi:10.1038/nphys2216](https://doi.org/10.1038/nphys2216)
  45. K. T. Law, P. A. Lee, T. K. Ng, Majorana fermion induced resonant Andreev reflection. *Phys. Rev. Lett.* **103**, 237001 (2009). [doi:10.1103/PhysRevLett.103.237001](https://doi.org/10.1103/PhysRevLett.103.237001) [Medline](#)
  46. S. M. Albrecht, A. P. Higginbotham, M. Madsen, F. Kuemmeth, T. S. Jespersen, J. Nygård, P. Krogstrup, C. M. Marcus, Exponential protection of zero modes in Majorana islands. *Nature* **531**, 206–209 (2016). [doi:10.1038/nature17162](https://doi.org/10.1038/nature17162)
  47. H. Zhang, C.-X. Liu, S. Gazibegovic, D. Xu, J. A. Logan, G. Wang, N. van Loo, J. D. S. Bommer, M. W. A. de Moor, D. Car, R. L. M. Op het Veld, P. J. van Veldhoven, S. Koelling, M. A. Verheijen, M. Pendharkar, D. J. Pennachio, B. Shojaei, J. S. Lee, C. J. Palmstrøm, E. P. A. M. Bakkers, S. D. Sarma, and L. P. Kouwenhoven, Quantized Majorana conductance. *Nature* **556**, 74–79 (2018). [doi:10.1038/nature26142](https://doi.org/10.1038/nature26142)
  48. B. E. Feldman, M. T. Randeria, J. Li, S. Jeon, Y. Xie, Z. Wang, I. K. Drozdov, B. Andrei Bernevig, A. Yazdani, High-resolution studies of the Majorana atomic chain platform. *Nat. Phys.* **13**, 286–291 (2016). [doi:10.1038/nphys3947](https://doi.org/10.1038/nphys3947)
  49. S. Jeon, Y. Xie, J. Li, Z. Wang, B. A. Bernevig, and A. Yazdani, Distinguishing a Majorana zero mode using spin-resolved measurements. *Science* **358**, 772–776 (2017). [doi:10.1126/science.aan3670](https://doi.org/10.1126/science.aan3670)
  50. D. I. Pikulin, J. P. Dahlhaus, M. Wimmer, H. Schomerus, C. W. J. Beenakker, A zero-voltage conductance peak from weak antilocalization in a Majorana nanowire. *New J. Phys.* **14**, 125011 (2012). [doi:10.1088/1367-2630/14/12/125011](https://doi.org/10.1088/1367-2630/14/12/125011)
  51. D. Bagrets and A. Altland, Class D Spectral Peak in Majorana Quantum Wires. *Phys. Rev. Lett.* **109**, 227005 (2012). [doi:10.1103/PhysRevLett.109.227005](https://doi.org/10.1103/PhysRevLett.109.227005)
  52. B. J. van Wees, P. de Vries, P. Magnée, T. M. Klapwijk, Excess conductance of superconductor-semiconductor interfaces due to phase conjugation between electrons and holes. *Phys. Rev. Lett.* **69**, 510 (1992). [doi:10.1103/PhysRevLett.69.510](https://doi.org/10.1103/PhysRevLett.69.510)
  53. E. J. H. Lee, X. Jiang, R. Aguado, G. Katsaros, C. M. Lieber, S. De Franceschi, Zero-bias anomaly in a nanowire quantum dot coupled to superconductors. *Phys. Rev. Lett.* **109**, 186802 (2012). [doi:10.1103/PhysRevLett.109.186802](https://doi.org/10.1103/PhysRevLett.109.186802) [Medline](#)
  54. H. O. H. Churchill, V. Fatemi, K. Grove-Rasmussen, M. T. Deng, P. Caroff, H. Q. Xu, C. M. Marcus, Superconductor-nanowire devices from tunneling to the multichannel regime: Zero-bias oscillations and magnetoconductance crossover. *Phys. Rev. B* **87**, 241401 (2013). [doi:10.1103/PhysRevB.87.241401](https://doi.org/10.1103/PhysRevB.87.241401)
  55. M. Ternes, W.-D. Schneider, J.-C. Cuevas, C. P. Lutz, C. F. Hirjibehedin, and A. J. Heinrich, Subgap structure in asymmetric superconducting tunnel junctions. *Phys. Rev. B* **74**, 132501 (2006). [doi:10.1103/PhysRevB.74.132501](https://doi.org/10.1103/PhysRevB.74.132501)
  56. N. Levy, T. Zhang, J. Ha, F. Sharifi, A. A. Talin, Y. Kuk, and J. A. Stroscio, Experimental Evidence for s-Wave Pairing Symmetry in Superconducting  $\text{Cu}_x\text{Bi}_2\text{Se}_3$  Single Crystals Using a Scanning Tunneling Microscope. *Phys. Rev. Lett.* **110**, 11701 (2013). [doi: 10.1103/PhysRevLett.110.117001](https://doi.org/10.1103/PhysRevLett.110.117001)
  57. F. Gygi and M. Schluter, Electronic tunneling into an isolated vortex in a clean type-II superconductor. *Phys. Rev. B* **41**, 822 (1990). [doi: 10.1103/PhysRevB.41.822](https://doi.org/10.1103/PhysRevB.41.822)

58. H. Nishimori, K. Uchiyama, S.-i. Kaneko, A. Tokura, H. Takeya, K. Hirata, and N. Nishida, First observation of the fourfold-symmetric and quantum regime vortex core in  $\text{YNi}_2\text{B}_2\text{C}$  by scanning tunneling microscopy and spectroscopy, *J. Phys. Soc. Jpn.* **73**, 3247 (2004). [doi: 10.1143/JPSJ.73.3247](https://doi.org/10.1143/JPSJ.73.3247)
59. J. Liu, F.-C. Zhang, and K. T. Law, Majorana fermion induced nonlocal current correlations in spin-orbit coupled superconducting wires. *Phys. Rev. B* **88**, 064509 (2013). [doi:10.1103/PhysRevB.88.064509](https://doi.org/10.1103/PhysRevB.88.064509)
60. G. E. Blonder, M. Tinkham, and T. M. Klapwijk, Transition from metallic to tunneling regimes in superconducting microconstrictions: Excess current, charge imbalance, and supercurrent conversion. *Phys. Rev. B* **25**, 4515 (1982). [doi: 10.1103/PhysRevB.25.4515](https://doi.org/10.1103/PhysRevB.25.4515)
61. L. Y. L. Shen and J. M. Rowell, Zero-Bias Tunneling Anomalies—Temperature, Voltage, and Magnetic Field Dependence. *Phys. Rev.* **165**, 566 (1968). [doi: 10.1103/PhysRev.165.566](https://doi.org/10.1103/PhysRev.165.566)
62. J. J. Cha, D. Kong, S.-S. Hong, J. G. Analytis, K. Lai, and Y. Cui, Weak antilocalization in  $\text{Bi}_2(\text{Se}_x\text{Te}_{1-x})_3$  nanoribbons and nanoplates. *Nano Letters* **12**, 1107-1111 (2012). [doi:10.1021/nl300018j](https://doi.org/10.1021/nl300018j)
63. V. Crespo, A. Maldonado, J. Galvis, P. Kulkarni, I. Guillamon, J. G. Rodrigo, H. Suderow, S. Vieira, S. Banerjee, P. Rodiere, Scanning microscopies of superconductors at very low temperatures. *Physica C* **479**, 19-23 (2012). [doi:10.1016/j.physc.2012.02.014](https://doi.org/10.1016/j.physc.2012.02.014)
64. T. Hanaguri, K. Kitagawa, K. Matsubayashi, Y. Mazaki, Y. Uwatoko, H. Takagi, Scanning tunneling microscopy/spectroscopy of vortices in  $\text{LiFeAs}$ . *Phys. Rev. B* **85**, 214505 (2012). [doi:10.1103/PhysRevB.85.214505](https://doi.org/10.1103/PhysRevB.85.214505)
65. N. Hayashi, T. Isoshima, M. Ichioka, and K. Machida, Low-Lying Quasiparticle Excitations around a Vortex Core in Quantum Limit. *Phys. Rev. Lett* **80**, 2921 (1998). [doi: 10.1103/PhysRevLett.80.2921](https://doi.org/10.1103/PhysRevLett.80.2921)
66. L. Shan, Y.-L. Wang, B. Shen, B. Zeng, Y. Huang, A. Li, D. Wang, H. Yang, C. Ren, Q.-H. Wang, S.H. Pan, and H.-H. Wen, Observation of ordered vortices with Andreev bound states in  $\text{Ba}_{0.6}\text{K}_{0.4}\text{Fe}_2\text{As}_2$ . *Nat. Phys.* **7**, 325-331 (2011). [doi:10.1038/nphys1908](https://doi.org/10.1038/nphys1908)
67. H. Hu, J.-M. Zuo, J. Wen, Z. Xu, Z. Lin, Q. Li, G. Gu, W. K. Park, and L. H. Greene, Phase separation in the iron chalcogenide superconductor  $\text{Fe}_{1+y}\text{Te}_x\text{Se}_{1-x}$ . *New J. Phys.* **13**, 053031 (2011). [doi:10.1088/1367-2630/13/5/053031](https://doi.org/10.1088/1367-2630/13/5/053031)
68. Ch. Renner and Ø. Fischer, Vacuum tunneling spectroscopy and asymmetric density of states of  $\text{Bi}_2\text{Sr}_2\text{CaCu}_2\text{O}_{8+\delta}$ . *Phys. Rev. B* **51**, 9208 (1995). [doi: 10.1103/PhysRevB.51.9208](https://doi.org/10.1103/PhysRevB.51.9208)
69. K. Flensberg, Tunneling characteristics of a chain of Majorana bound states. *Phys. Rev. B* **82**, 180516 (2010). [doi:10.1103/PhysRevB.82.180516](https://doi.org/10.1103/PhysRevB.82.180516)



### IN SCIENCE JOURNALS

Edited by **Stella Hurtley**

#### PLANT SCIENCE

### Poppy genome reveals evolution of opiates

**T**he opium poppy has been a source of painkillers since Neolithic times. Attendant risks of addiction threaten many today. Guo *et al.* now deliver a draft of the opium poppy genome, which encompasses 2.72 gigabases assembled into 11 chromosomes and predicts more than 50,000 protein-coding genes. A particularly complex gene cluster contains many critical enzymes in the metabolic pathway that generates the alkaloid drugs noscapine and morphinan. —PJH

*Science*, this issue p. 343



*Papaver somniferum*, the opium poppy

#### GRAPHENE

### Thickness matters in graphene stacks

If you stack graphene monolayers on top of each other, the number of layers will affect the properties of the material. Intuitively, one would expect that as the stack becomes thicker, the results will converge as the sample starts to resemble graphite. Nam *et al.* measured the conductance of graphene multilayers of increasing thickness. Studying

samples up to seven layers thick, they found that in all of them, electronic correlations caused a phase transition at a nonzero critical temperature. However, the critical temperature, as well as the nature of the low-temperature state, depended strongly on the number of layers. This unexpectedly persistent dependence showed no signs of slowing down and will motivate further theoretical and experimental work. —JS

*Science*, this issue p. 324

#### GEOPHYSICS

### A solid and squishy inner core

Earth's inner core is thought to be solid, which means it should support shear waves. However, the small size of the inner core makes detecting shear waves very difficult. Tkalčić and Pham correlated different types of seismic phases to finally determine the speed of shear waves in Earth's inner core (see the Perspective by Irving). The detection of the waves closes

an 80-year quest to find them and confirms a solid, but soft, inner core. —BG

*Science*, this issue p. 329; see also p. 294

#### SCIENCE AND SOCIETY

### Sharing pharmaceutical research

Increased collaboration will enhance our ability to predict new therapeutic drug candidates. Such data sharing is currently limited by concerns about intellectual property and competing commercial interests. Hie *et al.* introduce an end-to-end pipeline, using modern cryptographic tools, for secure pharmacological collaboration. Multiple entities can thus securely combine their private datasets to collectively obtain more accurate predictions of new drug-target interactions. The computational pipeline is practical, producing results with improved accuracy in a few days over a wide area network on a real dataset with more than a million interactions. —BJ and AMS

*Science*, this issue p. 347

#### IMMUNOLOGY

### The absence of DNGR-1 is dangerous

Conventional type 1 dendritic cells (cDC1s) can sense tissue damage via DNGR-1, which binds F-actin exposed by necrotic cells. DNGR-1 activation favors cross-presentation, the process by which extracellular antigens are processed and presented to CD8<sup>+</sup> T cells via major histocompatibility complex class I molecules. Del Fresno *et al.* studied mice lacking DNGR-1

and found that DNGR-1 also has anti-inflammatory effects (see the Perspective by Salazar and Brown). It inhibits the secretion of the chemokine CXCL2 by cDC1s, which, in turn, limits neutrophil recruitment. Thus, DNGR-1 connects cell-death sensing with a mechanism of damage control. —STS

*Science*, this issue p. 351;  
see also p. 292

## MALARIA

### Prenatal *Plasmodium* reactivity

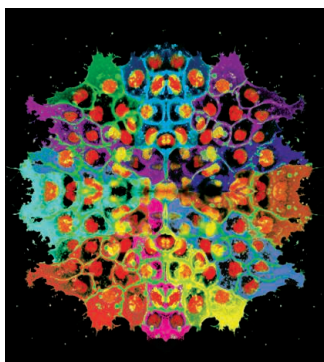
Fetal immunity is generally thought to be skewed toward tolerance. Odorizzi *et al.* used samples from a study in Uganda to determine if placental malaria infection modulated fetal immune responses to malaria. They stimulated cord blood cells in vitro and found that the fetal cells from cases of placental malaria were more reactive to *Plasmodium* antigens. Moreover, clinical follow-up revealed that this increased T cell response correlated with protection from childhood malaria. Thus, protective immune responses in humans can develop even before birth. —LP

*Sci. Transl. Med.* **10**, eaat6176 (2018).

## NEURODEVELOPMENT

### Supracellular cable drives collective cell movement

Neural crest cells migrate far and wide through a vertebrate embryo during development. Shellard *et al.* used *Xenopus*



Supracellular organization during collective migration

and zebrafish embryos to study how these clumps of mesenchymal cells migrate (see the Perspective by Adameyko). Movement was powered by a supracellular actomyosin cable that contracted around the rear of the clump. Similar supracellular contractility at the front was inhibited by a chemotactic signal. The imbalance in forces caused cells to rearrange so that the whole clump would be propelled forward. —PJH

*Science*, this issue p. 339;  
see also p. 290

## PAIN

### Channeling metastasis pain with VEGF

Metastatic cancer in the bone is painful. Yang *et al.* found that vascular endothelial growth factor (VEGF) promotes tumor angiogenesis and also contributes to this pain. In a rat model of bone-metastatic breast cancer, tumor-secreted VEGF repressed the expression of the potassium (K<sup>+</sup>) channel TRESK. Loss of K<sup>+</sup> current through TRESK increased the excitability of sensory neurons and made the animals hypersensitive to heat and touch near the bone lesion. Blocking this pathway restored channel activity and alleviated pain. —LKF

*Sci. Signal.* **11**, eaa05150 (2018).

## OPTICAL METAMATERIALS

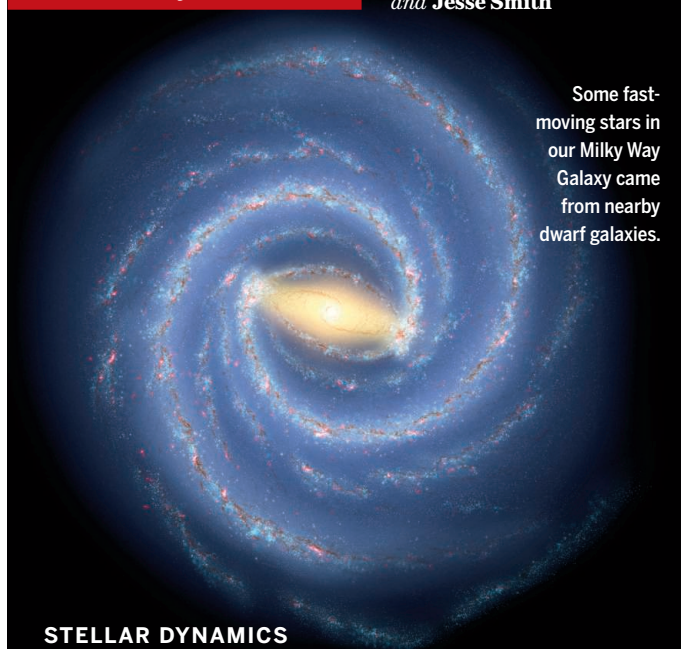
### Painting on the cool

Passive radiative cooling materials emit heat. They can reduce the need for air conditioning by providing daytime cooling but are often challenging to apply to rooftops and other building surfaces. Mandal *et al.* fabricated porous poly(vinylidene fluoride-co-hexafluoropropene) to create an excellent radiative cooling material. Better yet, the polymer is easy to paint or spray onto a wide range of surfaces, has good durability, and can even be dyed. This makes it a promising candidate for widespread use as a high-performance passive radiative cooling material. —BG

*Science*, this issue p. 315

## IN OTHER JOURNALS

Edited by **Caroline Ash**  
and **Jesse Smith**



Some fast-moving stars in our Milky Way Galaxy came from nearby dwarf galaxies.

## STELLAR DYNAMICS

### Fast-moving stars from other galaxies

**D**ynamical interactions and supernovae can accelerate stars to high velocities, sometimes even fast enough that they are no longer gravitationally bound to their host galaxy and escape from it. Marchetti *et al.* have combined astrometric data with radial velocity measurements to determine the three-dimensional motions of 7 million stars within the Milky Way Galaxy. Within that sample, they identify 20 stars that are not bound to the Galaxy. Only seven of them are moving away from the Milky Way's disc; 13 stars originated elsewhere. The authors postulate that these apparently extragalactic stars may have been ejected or tidally stripped from nearby dwarf galaxies. —KTS

*Mon. Not. R. Astron. Soc.* **10.1093/mnras/sty2592** (2018).

## VIRAL HOST RESPONSE

### Stressed out by influenza virus

Viral infection leads to cellular stress. This can act to the host's advantage to curb infection; however, the virus can also subvert stress responses for its own gain. Zhao *et al.* found that influenza A virus (IAV) infection leads to global deregulation of transcription. After IAV infection, RNA polymerase II runs through the transcription termination site of almost all active genes. This down-regulates gene expression by affecting the splicing of some transcripts and delaying the next rounds of

transcription initiation. The viral protein NS1 is responsible for this effect and can be modulated by SUMOylation. Although whether this stress response tilts in favor of host survival or facilitates viral replication is unknown, it might help explain the differences in pathogenicity seen in different IAV strains with divergent NS1. —SYM

*Nat. Struct. Mol. Biol.* **25**, 885 (2018).

## GENETIC DISEASE

### Impaired constriction

Duchenne muscular dystrophy (DMD) is a hereditary disease caused by mutations in the gene that encodes the protein

**QUANTUM INFORMATION****The stages of a quantum internet**

As indispensable as the internet has become in our daily lives, it still has many shortcomings, not least of which is that communication can be intercepted and information stolen. If, however, the internet attained the capability of transmitting quantum information—qubits—many of these security concerns would be addressed. Wehner *et al.* review what it will take to achieve this so-called quantum internet and propose stages of development that each correspond to increasingly powerful applications. Although a full-blown quantum internet, with functional quantum computers as nodes connected through quantum communication channels, is still some ways away, the first long-range quantum networks are already being planned. —JS

*Science*, this issue p. 303

**CONSERVATION****A nature-friendly matrix**

As the human population has grown, we have taken and modified more and more land, leaving less and less for nonhuman species. This is clearly unsustainable, and the amount of land we protect for nature needs to be increased and preserved. However, this still leaves vast regions of the world unprotected and modified. Such landscapes do not have to be a lost cause. Kremen and Merenlender review how biodiversity-based techniques can be used to manage most human-modified lands as “working landscapes.” These can provide for human needs and maintain biodiversity not just for ecosystem services but also for maintenance and persistence of nonhuman species. —SNV

*Science*, this issue p. 304

**ION CHANNELS****Structures of voltage-gated sodium channels**

In “excitable” cells, like neurons and muscle cells, a difference in electrical potential is used to transmit signals across the cell membrane. This difference is regulated by opening or closing ion channels in the cell membrane. For example, mutations in human voltage-gated sodium ( $\text{Na}_v$ ) channels are associated with disorders such as chronic pain, epilepsy, and cardiac arrhythmia. Pan *et al.* report the high-resolution structure of a human  $\text{Na}_v$  channel, and Shen *et al.* report the structures of an insect  $\text{Na}_v$  channel bound to the toxins that cause pufferfish and shellfish poisoning in humans. Together, the structures give insight into the molecular basis of sodium ion permeation and provide a path toward structure-based drug discovery. —VV

*Science*, this issue p. 305, p. 306

**SOCIAL SCIENCE****Assessing gender differences**

What contributes to gender-associated differences in preferences such as the willingness to take risks, patience, altruism, positive and negative reciprocity, and trust? Falk and Hermle studied 80,000 individuals in 76 countries who participated in a Global Preference Survey and compared the data with country-level variables such as gross domestic product and indices of gender inequality. They observed that the more that women have equal opportunities, the more they differ from men in their preferences. —BJ

*Science*, this issue p. 307

**QUANTUM COMPUTING****Quantum outperforms classical**

Quantum computers are expected to be better at solving certain computational problems than classical computers. This expectation is based on (well-founded) conjectures in computational complexity theory, but rigorous comparisons between the capabilities of quantum and classical algorithms are difficult to perform. Bravyi *et al.* proved theoretically that whereas the number of “steps” needed by parallel quantum circuits to solve certain linear algebra problems was independent of the problem size, this number grew logarithmically with size for analogous classical circuits (see the Perspective by Montanaro). This so-called quantum advantage stems from the quantum correlations present in quantum circuits that cannot be reproduced in analogous classical circuits. —JS

*Science*, this issue p. 308;

see also p. 289

**ORGANIC CHEMISTRY****Carbon nanotubes help nickel work in water**

Most synthetic chemistry takes place in hydrocarbon-derived solvents. By contrast, enzymes manage to perform exquisitely selective reactions in water, often by surrounding reactants with hydrophobic pockets. Kitano *et al.* show that single-walled carbon nanotubes can similarly render simple nickel catalysts effective in water. Integration of the nickel ions with chiral ligands and surfactants at the nanotube surface produces a highly enantioselective catalyst for nitro formation from aldoximes and unsaturated ketones. Spectroscopy suggests that the nanotubes enhance electron density at the nickel center as well as provide a hydrophobic milieu. —JSY

*Science*, this issue p. 311

**CHEMICAL SENSING****Transistor sensing in salt solutions**

Molecular binding to receptors on the surface of field-effect transistors (FETs) can be sensed through changes in transconductance. However, the saline solutions typically used with biomolecules create an electrical double layer that masks any events that occur within about 1 nanometer from the surface. Nakatsuka *et al.* overcame this limitation by using binding to large, negatively charged DNA stem loop structures that, upon ligand binding, cause conformational changes that can be sensed with an FET, even in solutions with high ionic strength. The authors demonstrate the sensing of charged molecules such as dopamine in artificial cerebrospinal fluid as well as neutral molecules such as glucose and zwitterion molecules like sphingosine-1-phosphate. —PDS

*Science*, this issue p. 319

**TOPOLOGICAL MATTER****An iron home for Majoranas**

The surface of the iron-based superconductor  $\text{FeTe}_{0.55}\text{Se}_{0.45}$  has been identified as a potential topological superconductor and is expected to host exotic quasiparticles called the Majorana bound states (MBSs). Wang *et al.* looked for signatures of MBSs in this material by using scanning tunneling spectroscopy on the vortex cores formed by the application of a magnetic field. In addition to conventional states, they observed the characteristic zero-bias peaks associated with MBSs and were able to distinguish between the two, owing to the favorable ratios of energy scales in the system. —JS

*Science*, this issue p. 333

## GERM CELL DEVELOPMENT

### Reconstituting a human ovary

Human pluripotent stem cells (hPSCs) have been induced into human primordial germ cell–like cells (hPGCLCs) in vitro, the first step toward human in vitro gametogenesis. Yamashiro *et al.* went a step closer to generating mature gametes by culturing hPSCs with mouse embryonic ovarian somatic cells in xenogeneic reconstituted ovaries (see the Perspective by Gill and Peters). Over a period of 4 months, hPGCLCs underwent hallmark epigenetic reprogramming and differentiated progressively into cells closely resembling human oogonia, an immediate embryonic precursor for human oocytes. This study creates opportunities for human germ cell research and provides a foundation for human in vitro gametogenesis. —BAP

*Science*, this issue p. 356;  
see also p. 291

## SUSTAINABILITY

### Policies to make you happy

Policy decision-making frequently involves economic models to assess their value. However, economic metrics do not tell the full story of how populations experience the policies implemented in their countries. In a Perspective, Graham *et al.* discuss the possible value of introducing well-being metrics—to assess factors influencing life satisfaction and happiness—to policy decision-making. They propose that including well-being considerations in policy-making could ensure future sustainability of the workforce. —GKA

*Science*, this issue p. 287

## ANTIGEN PRESENTATION

### Stitching peptides for presentation

Intracellular protein–derived peptides generated by proteasomal degradation are loaded onto major histocompatibility complex (MHC) class I molecules in the endoplasmic reticulum and presented to CD8<sup>+</sup> T cells. Although it has been assumed that these peptides are contiguous segments derived from intracellular proteins, recent studies have shown that noncontiguous peptides generated by cis-splicing of two distinct regions of an antigen can be presented by MHC class I molecules. Faridi *et al.* now demonstrate that MHC class I molecules can present peptides that are generated by the splicing together of segments from two distinct proteins—so-called trans-spliced peptides. Precisely how cis- and trans-spliced peptides are generated and how they contribute to T cell selection and expansion remain to be explored. —AB

*Sci. Immunol.* **3**, eaar3947 (2018).

## MAGNETIC RESONANCE

### Hyperfine spectra of surface atoms

The interaction of nuclei with nonzero spin with electron spins creates small electronic energy. With a scanning tunneling microscope tip, Willke *et al.* measured these hyperfine interactions for iron and titanium atoms that were manipulated on a magnesium oxide surface. The tip was also used to measure electron paramagnetic resonance spectra. The hyperfine structure of single atoms was sensitive to the binding site of the atom as well as its position relative to other magnetic atoms. —PDS

*Science*, this issue p. 336

# Science

## An iron home for Majoranas

Jelena Stajic

*Science* **362** (6412), 300-302.  
DOI: 10.1126/science.362.6412.300-q

### ARTICLE TOOLS

<http://science.sciencemag.org/content/362/6412/300.17>

### RELATED CONTENT

<file:/content/sci/362/6412/twis.full>

### PERMISSIONS

<http://www.sciencemag.org/help/reprints-and-permissions>

Use of this article is subject to the [Terms of Service](#)

---

*Science* (print ISSN 0036-8075; online ISSN 1095-9203) is published by the American Association for the Advancement of Science, 1200 New York Avenue NW, Washington, DC 20005. 2017 © The Authors, some rights reserved; exclusive licensee American Association for the Advancement of Science. No claim to original U.S. Government Works. The title *Science* is a registered trademark of AAAS.